

1 **Main Manuscript for**

2 **Increasing anthropogenic emissions inconsistent with declining**
3 **atmospheric mercury concentrations**

4
5 Aryeh Feinberg^{a*}, Noelle E. Selin^{a,b}, Christine F. Braban^c, Kai-Lan Chang^{d,e}, Danilo Custódio^f, Daniel A.
6 Jaffe^{g,h}, Katriina Kyllönenⁱ, Matthew S. Landis^j, Sarah R. Leeson^c, Koketso M. Molepo^k, Marijana
7 Murovec^l, Michelle G. Nerentorp Mastromonaco^m, Katrine Aspmo Pfaffhuberⁿ, Julian Rüdiger^o, Guey-
8 Rong Sheu^p, and Vincent L. St.Louis^q

9 ^a *Institute for Data, Systems, and Society, Massachusetts Institute of Technology, Cambridge, MA 02139,*
10 *USA*

11 ^b *Department of Earth, Atmospheric, and Planetary Sciences, Massachusetts Institute of Technology,*
12 *Cambridge, MA 02139, USA*

13 ^c *UK Centre for Ecology & Hydrology (UKCEH), Penicuik, Midlothian EH26 0QB, UK*

14 ^d *Cooperative Institute for Research in Environmental Sciences, University of Colorado, Boulder, CO*
15 *80309-0401, USA*

16 ^e *NOAA Chemical Sciences Laboratory, Boulder, CO 80305, USA*

17 ^f *Max-Planck-Institut für Biogeochemie, D-07745 Jena, Germany*

18 ^g *School of STEM, University of Washington Bothell, Bothell, WA 98011, USA*

19 ^h *Department of Atmospheric Sciences, University of Washington Seattle, Seattle, WA 98195, USA*

20 ⁱ *Finnish Meteorological Institute, Helsinki 00560, Finland*

21 ^j *United States Environmental Protection Agency, Office of Research and Development, Research*
22 *Triangle Park, NC 27711, USA*

23 ^k *Institute of Coastal Environmental Chemistry, Helmholtz Zentrum Hereon, 21502 Geesthacht, Germany*

24 ^l *Slovenian Environment Agency, Environment and Nature protection Office, Air Quality Division, 1000*
25 *Ljubljana, Slovenia*

26 ^m *IVL Swedish Environmental Research Institute, SE-411 33 Gothenburg, Sweden*

27 ⁿ *NILU, 2027 Kjeller, Norway*

28 ^o *Air Monitoring Network, German Environment Agency, 63225 Langen, Germany*

29 ^p *Department of Atmospheric Sciences, National Central University, Taoyuan 320, Taiwan*

30 ^q *Department of Biological Sciences, University of Alberta, Edmonton, AB T6G 2E9, Canada*

31

32 *Correspondence to: arifeinberg@gmail.com (A.F.)

33

34

35 **Author Contributions:** A.F. and N.E.S. designed the research. K.-L.C. advised the implementation of
36 statistical methods. C.F.B., D.C., D.A.J., K.K., M.S.L., S.R.L., K.M.M., M.M., M.G.N.M., K.A.P., J.R., G.-
37 R.S., and V.L.S.L. contributed Hg observation data. A.F. performed the analysis and wrote the manuscript
38 under the supervision of N.E.S., with inputs and discussion from all authors. Author order is alphabetical
39 following the second author, N.E.S.

40

41 **Competing Interest Statement:** The authors declare no competing interests.

42

43 **Classification:** Physical Sciences/Earth, Atmospheric, and Planetary Sciences

44

45 **Keywords:** mercury trends; anthropogenic emissions; atmospheric observations; Minamata Convention
46 on Mercury; biogeochemical box model; chemistry-transport model.

47

48 **This PDF file includes:**

49 Main Text

50 Figures 1 to 4

51

52 **Abstract (250 words)**

53 Anthropogenic activities emit $\sim 2000 \text{ Mg yr}^{-1}$ of the toxic heavy metal mercury (Hg) into the atmosphere,
54 where it can be transported long distances and deposited to remote ecosystems. Existing global
55 anthropogenic emissions inventories report increases in Northern Hemispheric (NH) Hg emissions during
56 the last three decades, in contradiction with the observed decline in atmospheric Hg concentrations at NH
57 measurement stations. Many factors can obscure the link between anthropogenic emissions and
58 atmospheric Hg concentrations, including trends in the re-emissions of previously released anthropogenic
59 (“legacy”) Hg, atmospheric sink variability, and spatial heterogeneity of monitoring data. Here we assess
60 the observed trends in total gaseous mercury (TGM) in the NH and apply biogeochemical box modeling
61 and chemical transport modeling to understand the trend drivers. Using linear mixed effects modeling of
62 observational data from 51 stations, we find negative TGM trends in most NH regions, with an overall
63 trend for 2005–2020 of $-0.011 \pm 0.006 \text{ ng m}^{-3} \text{ yr}^{-1}$ ($\pm 2 \text{ SD}$). We attribute this trend to a decline in NH
64 anthropogenic emissions of at least 165 Mg yr^{-1} between the years 2005 and 2020, using an ensemble of
65 simulations in a biogeochemical box model. Faster declines in 95th percentile TGM values than median
66 values in Europe, North America, and East Asian measurement stations corroborate that the likely cause
67 is a decline in nearby anthropogenic emissions rather than background legacy re-emissions. Our results
68 are relevant for evaluating the effectiveness of the Minamata Convention on Mercury and demonstrate
69 that existing emissions inventories are incompatible with the observed TGM declines.

70

71 **Significance statement (120 words)**

72 Mercury (Hg) is a global pollutant that bioaccumulates to toxic levels along the food chain. Anthropogenic
73 Hg inventories suggest increasing global emissions over recent decades, which is at odds with observed
74 declines of atmospheric Hg concentrations in the Northern Hemisphere (NH). We use statistical and
75 process-based modeling to rule out the possibility that NH anthropogenic emissions of Hg could have
76 increased while atmospheric Hg concentrations declined. This implies that anthropogenic emissions of Hg
77 have very likely declined in recent years. This work informs the effectiveness evaluation of the
78 international Minamata Convention on Mercury. Further research is required to better link emission
79 changes with measured concentrations so that the specific causes of global Hg trends can be identified.

80

81 **Main Text**

82

83 **Introduction**

84 The global Minamata Convention on Mercury is a multilateral environmental agreement that aims to
85 “protect human health and the environment from anthropogenic emissions and releases of mercury”, a
86 neurotoxic heavy metal (1). As mercury (Hg) is volatile and long-lived (~ 6 months) in the atmosphere (2),
87 trends in atmospheric mercury levels (Hg) are one of the proposed indicators that will be used to evaluate
88 the Convention’s effectiveness (3). However, linking trends in Hg concentrations and anthropogenic
89 emissions is not a straightforward process. The major anthropogenic emissions sources of Hg, including
90 artisanal and small-scale gold mining (ASGM), coal combustion, and industrial processes, are distributed
91 heterogeneously across the globe (4, 5). At the same time, legacy re-emissions of historical
92 anthropogenic mercury from soils, freshwater, wildfires, and oceans are diffuse background sources,
93 which are thought to make up a larger fraction of the overall Hg source fluxes (60% for legacy re-
94 emissions vs. 27% for primary anthropogenic) (6). Atmospheric Hg monitoring stations are also not evenly
95 distributed globally, with more stations located in North America and Europe (7), and they cover different
96 time periods. Therefore, statistical modeling is necessary to maximize the information present in
97 atmospheric Hg records (8), while mechanistic modeling helps connect observed Hg concentrations with
98 their drivers, i.e., emissions, transformations, transport, and deposition (7).

99

100 The large-scale trends of atmospheric Hg over the last three decades have been under recent debate.
101 Bottom-up inventories show increasing global anthropogenic emissions since the 1990s (5, 9, 10), which,
102 all else being equal, should increase atmospheric Hg levels. However, in North America and Europe,
103 measured total gaseous mercury (TGM) concentrations have generally been declining since continuous
104 measurements began in the 1990s (7, 11–13). There is a clear need to understand this contradiction and
105 evaluate past trends of Hg emissions, especially after the adoption of the Minamata Convention in 2013.
106 Zhang et al. (7), the most recent study to evaluate the consistency between emission inventories and
107 atmospheric observations using the chemical-transport model GEOS-Chem, analyzed available data
108 through 2014. Their comparison between the model and measurements from North America and Europe
109 led the authors to conclude that anthropogenic Hg emissions declined by ~30% between 1990 and 2010,
110 due to weaker increases of Hg emissions from ASGM and strong declines in Hg emissions from
111 commercial products (7). Measurement time series from East Asia have become more available recently,
112 with declines reported for atmospheric Hg (14–17). Long term measurements from the Southern
113 Hemisphere (SH) remain scarce, with the latest results from the observation stations Cape Point and
114 Amsterdam Island showing insignificant trends between 2012–2017 (18). Alternative hypotheses have
115 been proposed to explain the decline in atmospheric Hg in the Northern Hemisphere (NH) while
116 anthropogenic emissions rise, including increased elemental mercury (Hg^0) uptake by vegetation (19) and
117 declining Hg emissions from ocean legacy re-emissions due to reduced anthropogenic inputs after the
118 1970s (20, 21). However, a decline in legacy emissions of Hg is difficult to reconcile with biogeochemical
119 box models, which suggest that legacy Hg emissions generally increase if anthropogenic emissions are
120 constant or increasing (22).

121
122 Here, we perform trend analyses on a compiled NH dataset (1992–2022) of ambient total gaseous
123 mercury (TGM) measurements and conduct biogeochemical box model and GEOS-Chem chemistry-
124 transport model simulations to identify emissions trends that would be compatible with observed
125 concentration trends. We focus on TGM measurements rather than gaseous oxidized mercury (GOM)
126 and wet deposition measurements, as past measurements of GOM may have been biased low (23) and
127 wet deposition is more strongly affected by meteorological variability (24). We derive trends not only in
128 the mean or median changes in TGM but also in other statistical quantiles (e.g., 95th percentile) using
129 quantile regression, which can provide additional information regarding the drivers of trends.

130 131 **Results and Discussion**

132 **Regional trends in observed TGM (1992–2022).** We analyzed TGM data from 51 long-term monitoring
133 stations across the NH (Fig. 1). To calculate trends over wider regions, we aggregated stations based on
134 Intergovernmental Panel on Climate Change (IPCC) regions (25) and calculated overall trends using
135 linear mixed effect modeling (Fig. 2A–K). Overall trends for all NH regions except Northwestern North
136 America are declining over the available measurement periods between 1992 and 2022, with declines
137 ranging between -0.007 and $-0.035 \text{ ng m}^{-3} \text{ yr}^{-1}$ (concentration units refer to standard temperature and
138 pressure, STP). Northwestern North America (Fig. 2J) is the only NH region to show a positive trend, but
139 this region only includes one measurement site (Little Fox Lake, Yukon, Canada). The positive trend in
140 Little Fox Lake has been previously attributed to increasing transport from East Asia or increasing wildfire
141 frequency in Western Canada (12). However, in our analysis, the East Asian region also shows declining
142 TGM concentrations over 2006–2022 (trend $-0.023 \pm 0.005 \text{ ng m}^{-3} \text{ yr}^{-1}$) (Fig. 2H). Declines have also
143 been observed in other published shorter term measurement records from China (16, 17, 26, 27). For the
144 regions with more available measurement stations, including Eastern North America (ENA, $n = 19$) and
145 Northern Europe (NEU, $n = 13$), we tested a nonlinear method of obtaining an overall regional trend using
146 generalized additive models (GAM) (8). The derived regional trends are robust, as both the linear and
147 nonlinear approaches of deriving regional trends yield similar declines in these regions for 2005–2020
148 (-0.01 to $-0.02 \text{ ng m}^{-3} \text{ yr}^{-1}$) (Supplemental Information, SI, Fig. S3).

149 We find an overall NH TGM decline of $-0.011 \pm 0.006 \text{ ng m}^{-3} \text{ yr}^{-1}$ (± 2 standard deviations) for the period
150 2005–2020 (Fig. 2L), calculated by averaging regional trends (Fig. 2A–K) weighted by the areas of
151 corresponding IPCC regions. By first aggregating site trends by region, we reduce inherent biases from
152 the uneven spatial distribution of sites (i.e., biasing toward the trends of Eastern North America and
153 Europe) (SI Fig. S1). Our results largely agree with a previous trend assessment conducted on data from
154 1990–2014 (7), which found regional declines in TGM of -0.6 to $-2\% \text{ yr}^{-1}$ (approximately corresponding to
155 -0.01 to $-0.03 \text{ ng m}^{-3} \text{ yr}^{-1}$). The current work benefits from improved statistical techniques to combine
156 information from multiple sites and a larger number of stations and regions covered in more recent time
157 periods. We have not included an analysis of SH regional trends in the current work due to the sparse
158 coverage of SH long-term monitoring stations (Fig. 1). From published information, two SH monitoring
159 stations (Cape Point, South Africa and Amsterdam Island) do not show significant trends during the
160 2012–2017 period, while Cape Point shows a positive trend of $\sim 0.008 \text{ ng m}^{-3} \text{ yr}^{-1}$ over 2007–2017 (18).
161 As the NH has a wider dataset of TGM time series and is the principal hemisphere for anthropogenic
162 emissions, we proceed with constraining Hg budget trends based on the NH trend in TGM.

163
164 **Constraining emissions trends for 2005–2020.** We ran 2×10^5 scenarios in a biogeochemical box
165 model for 2005–2020, varying 19 Hg budget parameters including the trends in anthropogenic emissions
166 and releases, the response of legacy emissions to recent and historical anthropogenic inputs, emissions
167 speciation trends, and the atmospheric Hg lifetime (Table S2). Figure 3A shows the response of the
168 2005–2020 trend in NH TGM to the 2005–2020 trend in total (anthropogenic + legacy) NH emissions.
169 Note that emissions fluxes are reported in Mg yr^{-1} , and thus trends in these fluxes are expressed as Mg
170 yr^{-2} . Our best estimate for the observed 2005–2020 trend in surface NH TGM is $-0.011 \pm 0.006 \text{ ng m}^{-3}$
171 yr^{-1} . However, to account for potential differences between NH surface and whole troposphere trends (SI
172 Section S3.1) we assumed an extended uncertainty range for NH tropospheric TGM trends from -0.017 to
173 $-0.004 \text{ ng m}^{-3} \text{ yr}^{-1}$ (grey shaded area in Figs. 3A and B). The NH total emissions trends that would be
174 compatible with the observed TGM trends ranges from -17 Mg yr^{-2} to more than -80 Mg yr^{-2} . This range is
175 consistent with a previous emissions trend estimate based on 1990–2010 observations (-610 Mg yr^{-1} total
176 difference; -30.5 Mg yr^{-2} trend) (7).

177
178 The relationship between TGM trends and NH anthropogenic emissions trends is associated with larger
179 uncertainties (Figure 3B) than that of total NH emissions (Figure 3A). The uncertainty range expands due
180 to additional uncertainties in the response of legacy emissions to anthropogenic inputs and the trends in
181 releases to water and land that would accompany anthropogenic emissions trends for 2005–2020. The
182 uncertainty range for observed NH troposphere TGM trends (-0.017 to $-0.004 \text{ ng m}^{-3} \text{ yr}^{-1}$) is compatible
183 only with anthropogenic emission trends that are declining by more than -11 Mg yr^{-2} . The positive NH
184 anthropogenic emissions trend estimated by the Streets et al. (10) inventory for 2005–2015 (34 Mg yr^{-2}),
185 should result in NH TGM increases on the order of $0.09 \text{ ng m}^{-3} \text{ yr}^{-1}$. Other global inventories are currently
186 limited in terms of their temporal coverage, yet the EDGAR inventory estimates an increase of 54 Mg yr^{-2}
187 over 2005–2012 in the NH (9) and the AMAP/UNEP inventory estimates an NH increase of 44 Mg yr^{-2}
188 between 2010 and 2015 (5). We conclude that current bottom-up inventories of anthropogenic Hg
189 emissions are inconsistent with the declines in observed NH TGM for 2005–2020.

190
191 Previous studies (20, 21) have hypothesized that NH TGM may be decreasing due to broad-scale
192 declines in legacy emissions, even as anthropogenic emissions increase or stay constant. However, our
193 biogeochemical box model analysis illustrates that it is very unlikely for legacy emissions to decrease if
194 recent (2005–2020) anthropogenic emissions are not also decreasing. Even if anthropogenic emissions
195 stay constant, legacy emissions will grow due to the increasing supply of Hg (22). This effect causes the
196 displacement of the intercept in Figure 3B, with the anthropogenic emissions trend needing to be below -8
197 Mg yr^{-2} for the median predicted TGM trend to become negative (Figure 3B). We explored the potential

198 impacts of errors in the historical emission and release inventories on recent the re-emissions trend
199 (Figure S5). If we assume underestimates in 1970 emissions and releases, when Hg discharges were at
200 their peak (28, 29), the recent re-emissions trend would be more negative (Figure S5A). However, the
201 degree to which the potential error in 1970 emissions affects the 2005–2020 re-emissions trend is smaller
202 than the impacts of more recent errors (1990, 2000), and a factor of ~15 smaller than the influence of
203 contemporary (2005–2020) anthropogenic emissions and releases trends (Figs. S5F and G). Therefore,
204 although historical emissions and releases play a role in the recent re-emissions trend, the dominant
205 factor for the recent re-emissions trend will be recent trends in anthropogenic Hg inputs to the
206 environment. Our results are robust to the uncertainties in the lifetimes of legacy Hg in the surface
207 environment (Table S2).

208
209 We explored the role of trend drivers other than anthropogenic inputs by repeating the sampling of the
210 box model throughout the parameter space, accounting for additional causes. If the oxidation lifetime of
211 Hg^0 declined between 2005–2020, it can become easier to reconcile the observed TGM decline with
212 positive anthropogenic emissions trends (Fig. 3C). However, the oxidation lifetime of Hg^0 would have to
213 decline by 14% for at least a 5% likelihood of positive anthropogenic emissions trends (i.e., when the
214 oxidation lifetime declines by 14% over 2005–2020, 5% of the simulations that are within the observed
215 NH TGM trend range have positive NH anthropogenic emissions trends). A hemispheric decrease in the
216 oxidation lifetime of this magnitude would be surprising for the 2005–2020 period, as modeling estimates
217 for the methane (CH_4) lifetime suggest only 9% declines over the longer period of 1980–2014, driven by
218 increases in hydroxyl radical (OH) concentrations (30). In addition, the two-step Hg oxidation chemistry
219 will be affected by other oxidants as well, including ozone, bromine radicals, and nitrogen oxides (2, 31–
220 33). Many of these oxidants are impacted by anthropogenic pollution sources that have trended differently
221 in different regions, and therefore are likely not the main factor between the consistent declines seen
222 across the NH. An increased oxidation rate would also have enhanced the sink of Hg through wet
223 deposition, as oxidation converts insoluble Hg^0 to soluble species. However, previous studies have
224 identified overall declines in wet deposition of Hg over North America (13, 34) and Europe (5).

225
226 Another potential factor is the increase in terrestrial primary production through global greening, which
227 Jiskra et al. (19) estimated increased the NH dry deposition of Hg^0 to vegetation by 7 Mg yr^{-2} between
228 1990 and 2010. However, the NH dry deposition sink would have to increase by unrealistic levels (20 Mg
229 yr^{-2}) to yield a 5% likelihood of positive anthropogenic emissions trends (Figure 3D). Other climate change
230 factors can play a role in recent legacy emissions trends, like release of Hg from melting permafrost (35),
231 changes to ocean evasion of Hg^0 through warming, acidification, and wind speed changes (36),
232 decreased sea ice coverage allowing further Hg^0 evasion (37), and enhanced wildfire emissions (38).
233 These identified climate feedbacks, however, tend to increase legacy Hg re-emissions, and thus could not
234 explain why anthropogenic emissions in bottom-up inventories increase while TGM trends decline.
235 Although further research into these factors is required to reduce uncertainties in recent trend drivers, our
236 conclusion remains that it is very unlikely that NH anthropogenic emissions could have increased or even
237 stayed constant over 2005–2020, with the TGM declines observed over this period in the NH.

238
239 **Spatial and quantile variability of TGM trends.** Although the box model is useful for constraining overall
240 hemispheric trends, it cannot capture the spatial heterogeneity of these trends driven by variability in
241 sources, sinks, and transport. We ran simulations in the 3-D chemical-transport model GEOS-Chem (39,
242 40) to investigate different emissions scenarios over the 2005–2020 period and calculated mean trends in
243 NH TGM using area-weighted averaging of observed regions (Fig. 4A). The BASE simulation, including
244 anthropogenic emissions increases according to Streets et al. (10) for 2005–2015 with constant
245 emissions after 2015, shows an increase in NH TGM of $0.005 \text{ ng m}^{-3} \text{ yr}^{-1}$. In the BASE+LEG simulation,
246 we considered the feedback of legacy emissions to increasing anthropogenic emissions, leading to a

247 stronger increase of $0.010 \text{ ng m}^{-3} \text{ yr}^{-1}$ in NH TGM. Echoing the box modeling results, we thus find that
248 increases in anthropogenic emissions found in existing inventories is inconsistent with the observed
249 trends in NH TGM, $-0.011 \pm 0.006 \text{ ng m}^{-3} \text{ yr}^{-1}$. We also simulated two potential scenarios for a decreasing
250 NH emissions trend: DEC_ANT, which includes a decline in South and East Asian emissions following
251 the trend in Chinese emissions inventories (41, 42), and DEC_LEG_ONLY, which considers declining
252 ocean re-emissions of Hg in the NH and SH. Both of these emission scenarios are within uncertainties of
253 the observed trend in mean NH TGM (DEC_ANT: $-0.007 \text{ ng m}^{-3} \text{ yr}^{-1}$; DEC_LEG_ONLY: -0.013 ng m^{-3}
254 yr^{-1}). Since it is difficult to understand the causes of the TGM decline based on the mean hemispheric
255 trend alone, we also assess the spatial and quantile variations in trends.

256
257 We use quantile regression to assess trends in the observed median (P50) and 95th percentile (P95)
258 deseasonalized daily TGM values. Fig. 4B maps the simulated P50 trends in BASE+LEG, showing
259 increasing concentrations across the globe, in disagreement with 8 of the 9 plotted stations (>13 years
260 observed between 2005 and 2020), which show declines. The difference between P95 trends and P50
261 trends (Fig. 4C) correlates with the change in anthropogenic emissions between 2005 and 2020 (SI Fig.
262 S7). BASE+LEG simulates P95 declining more than P50 in Eastern North America and Central Europe
263 (areas of emissions decreases), while P95 increases more than P50 in East Asia and South Africa (areas
264 of emissions increases). Available high-resolution measurement records confirm the simulated P95 – P50
265 trends in Eastern North America (Egbert and Kejimkujik) and Europe (Mace Head, Schmücke, and
266 Pallas), yet they also show declines in East Asia (Cape Hedo). The DEC_ANT simulation, where South
267 and East Asian anthropogenic emissions decline, succeeds in matching the observed signal in P95 – P50
268 trends (Fig. 4E), whereas the DEC_LEG_ONLY simulation, in which legacy emissions decline, shows
269 similar patterns to BASE+LEG and disagrees with Cape Hedo observations (Fig. 4G). Therefore, despite
270 showing similar P50 trends (Figs. 4D and F) in NH TGM, DEC_ANT and DEC_LEG_ONLY can be
271 distinguished by simulated patterns in quantile trends. The current results support findings from Hg
272 measurement studies in the 1990s (43, 44), which suggested that reductions in observed extreme
273 concentrations could be useful indicators for regional emissions changes. Incorporation of quantile trends
274 as constraints in Hg modeling can thus help maximize the information provided by high resolution
275 monitoring stations.

276

277 **Implications for the drivers of atmospheric Hg trends.**

278 Observed TGM is generally declining in most NH regions, with an estimated hemispheric trend of $-0.011 \pm$
279 $0.006 \text{ ng m}^{-3} \text{ yr}^{-1}$ for 2005–2020. By testing a large ensemble of parameters using box modeling and
280 comparing with available measurements of atmospheric concentrations, we showed that NH
281 anthropogenic emissions likely declined by more than -165 Mg yr^{-1} (-11 Mg yr^{-2}) over this period (Fig. 3B).
282 This result is at odds with existing anthropogenic emissions inventories (5, 9, 10), which all show NH
283 increases of larger than 34 Mg yr^{-2} , although no inventory yet covers the full 2005–2020 period. Thus,
284 there is a potential gap of 45 Mg yr^{-2} ($\sim 675 \text{ Mg yr}^{-1}$) between estimated anthropogenic emissions trends
285 from inventories and trends expected from observed TGM trends. This gap could quantitatively be
286 impacted (in both directions) by global change factors like the Hg^0 oxidation lifetime and vegetation sink,
287 yet it is unlikely to be substantially reduced (Fig. 2C–D). Our DEC_ANT simulation showed that this gap
288 could be explained by a decline in South and East Asian emissions, reflecting more detailed information
289 for air pollution control device efficiencies from Chinese national inventories (41, 42, 45). The hypothesis
290 of declining East Asian emissions is supported by the observed decline in P95 TGM concentrations at
291 Cape Hedo (Fig. 4E), along with observed declines in mean TGM values from other East Asian stations
292 (Fig. 2H). However, other anthropogenic emissions sources are also associated with large uncertainties,
293 which could contribute to the gap between inventories and measurement-derived emissions trends. For
294 example, ASGM is currently thought to be the largest yet highly uncertain source (globally 775 Mg yr^{-1} in
295 2015) of anthropogenic Hg emissions (10), and estimated trends in this source can differ depending on

296 whether it is estimated to change with time following different proxies such as gold demand or poverty
297 (10, 46). High uncertainties are also linked with emissions from Hg-containing products (globally 436 Mg
298 yr^{-1}) (10), as the magnitudes of historically produced Hg are large (~ 1000 Gg) and emissions factors as
299 well as timescales are uncertain (47). Measurement constraints are limited, and our four tested GEOS-
300 Chem simulations were not designed to cover the entire potential uncertainty space in emissions, so we
301 cannot further identify the source types responsible for the discrepancy between emissions inventory and
302 observed trends. Nevertheless, both our box and GEOS-Chem modeling analyses suggest that a decline
303 in legacy emissions in the absence of anthropogenic emissions reductions is unlikely given our
304 understanding of the Hg cycle and measured quantile trends.

305
306 The levels of uncertainty in anthropogenic emissions and biogeochemical cycling of Hg emphasizes the
307 need for continued assessment of inventories and models based on available observations and emerging
308 constraints like Hg isotopes (48). Expansion of the current monitoring network in strategic locations would
309 be valuable for trend quantification and attribution to sources. For example, existing SH measurement
310 locations are largely influenced by marine rather than anthropogenic sources (49, 50), with no long-term
311 measurement stations located nearby ASGM activities (Fig. 1). We focused here on trends in TGM in the
312 NH due to the increased prevalence of NH anthropogenic emissions and monitoring, but further
313 monitoring of atmospheric Hg in the SH is essential for constraining trends in Hg sources. For example,
314 major differences between the simulated DEC_ANT and DEC_LEG_ONLY median trends occur in the
315 SH (Fig. 4). Passive samplers (51) can enable economical Hg monitoring in remote locations, yet active
316 continuous sampling will continue to deliver the benefits of higher time resolution (e.g., atmospheric
317 dynamics, source identification) compared to passive samplers (\sim monthly resolution). Here we showed
318 that the trends in the statistical distribution of TGM, which can only be facilitated by active sampling
319 methods, are a useful indicator of which sources are changing. Reduced-form models (52, 53) and tools
320 to produce emissions inventories from socioeconomic data more quickly (54), which have been applied
321 extensively in the climate and air pollution fields, can enable more up-to-date evaluations of the latest Hg
322 trends and drivers. Improvements in Hg models, including the response of legacy re-emissions to
323 anthropogenic emissions scenarios and global change factors, will be essential for further analysis of Hg
324 trends. The planned analysis to support the Minamata Convention effectiveness evaluation will advance
325 this approach by investigating the drivers of Hg trends in multiple Hg models (3). As declining
326 atmospheric Hg inputs to ecosystems can directly impact levels of Hg in biota (55), understanding the
327 trends in atmospheric Hg burden is essential for better predictions of how Hg pollution will evolve under
328 future regulatory control scenarios and climate change.

329 330 **Materials and Methods**

331 **Atmospheric mercury observations.** Atmospheric mercury (Hg) occurs as different species: the volatile
332 species gaseous elemental mercury (GEM: Hg^0), the soluble, shorter-lived species gaseous oxidized
333 mercury (GOM: Hg^I and Hg^{II}), and particulate-bound mercury (Hg^P). We compiled data from 51 stations
334 which have more than 6 years of measurements of GEM or total gaseous mercury (TGM = GEM + GOM)
335 in the period 1992 to 2022 (Table S1). Similar to previous trend studies (7, 12), we do not differentiate
336 between TGM and GEM measurements, as TGM is $>98\%$ GEM under usual conditions (23). We
337 analyzed data from multiple measurement networks: the US Atmospheric Mercury Network (AMNet) (56),
338 Canadian Air and Precipitation Monitoring Network (CAPMoN) (34), European Monitoring and Evaluation
339 Programme (EMEP) (57), Global Mercury Observation System (GMOS) (58), Ministry of Environment
340 Japan (MOEJ) (14), Ministry of Environment (MOENV) Taiwan (15), and the Experimental Lakes Area
341 (59). We also included a Mauna Loa measurement dataset from the US EPA from 2002 to 2009 (60, 61),
342 which later transitioned into an AMNet site. Most TGM and GEM measurements were made with Tekran
343 Instruments Corporation (Toronto, Canada) Models 2537A/X systems, which capture ambient Hg by gold
344 trap amalgamation, subsequently thermally desorbing this accumulated Hg to be detected by Cold

345 Vapour Atomic Fluorescence Spectrometry (CVAFS) (61). Two sites in the EMEP network (Iskrba after
 346 2017 and Lahemaa) employed Lumex Instruments (St. Petersburg, Russia) Model RA-915 mercury
 347 analyzers, which detect GEM through Zeeman Atomic Absorption Spectrometry using High Frequency
 348 Modulated light polarisation (ZAAS-HFM) (62). Before 2017, TGM was measured at Iskrba with Mercury
 349 Instruments Analytical Technologies (Karlsfeld, Germany) Model UT-3000 analyzers using cold vapor
 350 atomic absorption spectroscopy (CVAAS). All the continuous TGM and GEM measurements are made at
 351 5–15 min intervals, which are averaged and reported hourly. Measurements from Zeppelin Station (before
 352 2000), Birkenes (before 2010), Lista, Råö, Bredkälen, Hallahus, and Pallas (the measurements from IVL,
 353 Swedish Environmental Research Institute) were made manually with a gold trap sampling technique
 354 (63). Data at lower frequencies (manual sites and the Auchencorth Moss and Iskrba timeseries) were
 355 used to compute monthly mean statistics for timeseries. At the sites with high-frequency measurements,
 356 daily mean values were calculated and used to compute means for all months with at least 10 daily
 357 values. All measurement and modeling data for TGM is reported in units of $\text{ng m}^{-3} \text{ yr}^{-1}$ at standard
 358 temperature and pressure (STP, 0 °C and 1 atm).

359
 360 **Statistical methods.** Monthly mean data were deseasonalized before trend analysis by fitting each
 361 station timeseries with four harmonic terms (64). In order to achieve a better evidence synthesis from
 362 individual site data, we focused our statistical analysis on calculating overall trends from wider regions.
 363 We chose to aggregate Hg trends based on the IPCC regions (Figure 1). These regions are standardly
 364 used in the atmospheric science community and are designed to have consistent climate features (25),
 365 providing advantages over using whole continent or country-based aggregations. There are 61 regions in
 366 total; we analyzed trends for 11 regions in the NH where stations measuring Hg over the long term were
 367 available. We aim to derive regionally representative trends by integrating information from all data
 368 sources, because individual sites might only provide a partial view of regional variations, as they cover
 369 different time periods, come from different measurement networks, include data gaps, and are potentially
 370 exposed to unique local sources and sinks. In previous studies on Hg trends, regional timeseries have
 371 been calculated by averaging all sites that are available in a particular year (7). However, this approach is
 372 biased when sites do not all cover the same time period, since offsets between mean site concentrations
 373 can affect the calculated trend results (SI Section S3.2). To address this heterogeneity, we explicitly
 374 modeled offsets and trend deviations between sites with linear mixed effects (LME) models (64, 65).
 375 Using LME models, a time series can be described with terms representing the consensus trend and
 376 intercept for a region (“fixed effect”) and terms representing site-level deviations (“random effect”).
 377 Individual sites were modeled using Eq. 1:

$$378 \quad y_k = a + bt + \alpha_k + \beta_k t \quad (\text{Eq. 1})$$

379 where y_k are deseasonalized monthly mean TGM values for each site, a is the regional intercept, b is the
 380 regional trend, α_k is the site offset, and β_k is the site deviation in trend. To account for autocorrelation, we
 381 assumed that residual site errors follow an AR(1) process. We calculated these trends using LME
 382 modeling in the R package lme4 (65). For the purposes of LME modeling, EPA and AMNet data for
 383 Mauna Loa, as well as Finnish Meteorological Institute (FMI) and Swedish Environmental Research
 384 Institute (IVL) data for Pallas, were treated as different sites (as different measurement networks may
 385 have offsets). We applied LME modeling to the nine NH regions where multisite data is available. For the
 386 two regions (Northwestern North America and the Arctic Ocean) where only one site is available, we
 387 calculated generalized least squares (GLS) trends with AR(1) errors on deseasonalized monthly mean
 388 values. We chose linear approaches for trend analysis as this follows recommendations for multisite
 389 analysis when only a few sites are available for a region (64). We found consistent results between LME
 390 trends and nonlinear trends calculated with generalized additive models (GAMs) for regions (Eastern
 391 North America and Northern Europe) where a larger number of sites (>12) are available (SI Fig. S3).

392

393 We weighted regional trends by the areas of the corresponding IPCC regions to calculate the overall NH
 394 trend, which allowed us to compare with box model simulations. The overall NH trend was calculated for
 395 2005–2020, which is the time period with the best availability of data from all 11 regions. The error in the
 396 NH trend was calculated through Monte Carlo sampling of regional trends ± 2 standard deviation.
 397 Analogous trend calculations were performed for GEOS-Chem simulated TGM values, which showed that
 398 NH trends derived from regional weighted averages were more representative of the true NH surface
 399 trend than averages of all available sites without regional aggregation (SI Fig. S1).

400
 401 For sites where high frequency TGM measurements are available, we additionally calculated quantile
 402 regression (QR) trends over the 2005–2020 period (66). Other atmospheric chemistry studies (8, 67, 68)
 403 have applied QR, as it enables the quantification of trends not only in the mean values but throughout the
 404 distribution of the observed quantity. Earlier studies have observed heterogeneous changes in the
 405 statistical distribution of atmospheric Hg measurements driven by emissions changes (43, 44), yet these
 406 have not been followed up with more modern statistical techniques. We analyzed deseasonalized daily
 407 mean values at these sites and calculated trends for 5th–95th percentiles, with errors derived using
 408 bootstrapping. We applied the R package quantreg for this analysis (69).

409
 410 **Box model simulations.** We used a 3-box model that considers atmospheric Hg⁰ and Hg^{II} in two
 411 tropospheric boxes (NH and SH) and one stratospheric box (70) to simulate potential scenarios for trends
 412 during 2005–2020. We constructed an ensemble of scenarios accounting for uncertainties in the
 413 atmospheric Hg lifetime, historical (pre-2005) anthropogenic emissions and releases, recent (2005–2020)
 414 anthropogenic emissions and releases, the response of legacy emissions to anthropogenic inputs, and
 415 recent (2005–2020) speciation trends. We assigned uncertainty ranges to these 19 parameters (SI Table
 416 S2) and sampled 2×10^5 scenarios within this parameter space, using Latin Hypercube Sampling (71).

417
 418 To address the response in legacy emissions to historical and recent anthropogenic inputs, we applied
 419 the effective anthropogenic mercury deposition (EAMD) concept (72). Our approach used two minor
 420 adaptations: (1) tracking the effective anthropogenic mercury emissions (EAME) instead of deposition
 421 (which leads to offsets of several months in lifetimes); and (2) using a two-term negative exponential
 422 model. Given primary emissions or releases of mercury in a specific year (ϵ_i), Eq. 2 calculates the EAME,
 423 in a future time t :

$$424 \quad \text{EAME}_i(t) = \epsilon_i \left(a_1 \exp\left(-\frac{t}{b_1}\right) + a_2 \exp\left(-\frac{t}{b_2}\right) \right) \quad (\text{Eq. 2})$$

425
 426 where a_1 and a_2 are coefficients and b_1 and b_2 are lifetimes representing the quick and slow re-emission
 427 processes, respectively. Total legacy emissions (E_{leg}) in the year t were calculated by summing up all
 428 EAME_{*i*} resulting from previous primary emissions using Eq. 3:

$$429 \quad E_{\text{leg}}(t) = \sum_{i < t} \text{EAME}_i \quad (\text{Eq. 3})$$

430
 431 We employed pulse experiments with parameter perturbations in the Hg Global Biogeochemical Box
 432 model (GBC) (6, 73) to calculate reasonable ranges for the a and b parameters (SI Section S4). We
 433 pulsed an additional 100 Mg Hg either emitted or released to rivers in 2010 and fit the resultant additional
 434 legacy re-emissions until 2110 using Eq. 2. We conducted these pulse experiments on 1000 iterations of
 435 the GBC model, varying each of the 40 rate coefficients and parameters within the GBC model within a
 436 factor of 2 using Latin Hypercube Sampling. We found that b_1 ranges between 6–15 months for
 437 atmospheric emissions and 2–10 months for releases, corresponding to the timescale of atmospheric
 438 deposition and re-emission from the surface ocean. The longer lifetime, b_2 , ranges between 29–97 years
 440

441 for atmospheric emissions and 1–117 years for releases, corresponding to the timescale of removal of Hg
442 from the atmosphere–surface ocean–subsurface ocean system through transfer to the deep ocean or
443 temporary storage in soils (6). Although longer time scales (~1000 yr) would be required to model burial
444 of Hg in the deep ocean, Eq. 2 covers the legacy re-emission response in near-future projections (<100
445 years), while having only 4 parameters as opposed to 40 parameters in the GBC model (72). We also
446 calculated ranges for the fraction of Hg re-emitted in the short timescale term and the total Hg re-
447 emissions resulting from a pulse, which can be used to calculate a_1 and a_2 in Eq. 2.
448

449 Anthropogenic emissions and releases of Hg were taken from the Streets et al. (29) inventory, which
450 covers decadal points over the historical period (1510–2010). We accounted for uncertainties in
451 emissions and releases for recent decadal points (1970, 1980, 1990, 2000, 2010) by applying
452 perturbations between –20% and +40% to these values, which is the suggested emission inventory
453 uncertainty range (10). We interpolated between the decadal points to calculate emissions with yearly
454 resolution between 1510–2005. For 2005–2020, we applied varying linear trends in anthropogenic
455 emissions for both hemispheres, restricting the trend range to ensure non-negative emissions in 2020.
456 The anthropogenic releases for 2005–2020 were calculated based on the historical relationship between
457 emissions and releases trends in the inventory (29), with random perturbations introduced for the
458 hemispheric release trends (SI Table S2). This procedure yielded 2×10^5 potential timeseries for
459 anthropogenic emissions and releases over 1510–2020. Combining these scenarios with varying sets of
460 legacy parameters (Eq. 2), we calculated the resultant global legacy re-emissions timeseries for 2005–
461 2020 for each of the 2×10^5 scenarios. For simplicity, the distribution of legacy re-emissions by
462 hemisphere was assumed to be constant over 2005–2020 based on the ratio in GEOS-Chem (44% NH,
463 55% SH; this is similar to the ratio of ocean coverage in the NH and SH). Speciation of the anthropogenic
464 emissions in 2005 was set to 65% Hg⁰ and 35% Hg^{II}; we applied a variable linear trend in speciation so
465 that speciation in 2020 ranged between 45% and 85% Hg⁰.
466

467 We ran the 2×10^5 scenarios in the 3-box model for 2005 to evaluate whether the sampled combinations
468 of emissions and atmospheric Hg lifetimes (ranging between 3–8 months) yield a reasonable Hg burden.
469 We rejected scenarios that yield a 2005 burden in the NH troposphere outside of the range 1600–3300
470 Mg (corresponding to average tropospheric concentrations of 0.8–1.6 ng m⁻³). Approximately 10^5 samples
471 passed this constraint, which we then utilized for full 2005–2020 box model runs. We evaluated linear
472 trends in NH TGM in each of these box model runs and compared these to the inputted total and
473 anthropogenic emission trends for 2005–2020.
474

475 To assess the impacts of other non-emissions factors in NH TGM trends, we repeated this procedure
476 accounting for potential trends in Hg⁰ dry deposition and oxidation. We re-ran the 2×10^5 scenarios with
477 linear trends in the dry deposition rate coefficient so that the value in 2020 varied between 100% to 170%
478 of its value in 2005. Similarly, we ran 2×10^5 scenarios with the Hg⁰ oxidation rate coefficient varying in
479 2020 between 100% and 200% of its value in 2005.
480

481 **GEOS-Chem simulations.** We ran 3-D atmospheric simulations for the 2005–2020 period in the
482 chemistry-transport model GEOS-Chem. We used version 12.8.1 of the Hg model (39) with improvements
483 in the dry deposition of Hg⁰ (70). The model was run globally at $2.0^\circ \times 2.5^\circ$ horizontal resolution and 47
484 vertical levels up to 0.01 hPa (80 km). The model was forced with offline meteorology from the MERRA-2
485 product (74). The model treats three species of Hg: elemental mercury (Hg⁰, GEM), oxidized mercury
486 (Hg^{II}, GOM), and particulate mercury (Hg^P). Oxidation of Hg⁰ occurs through a two-step mechanism
487 initiated by atomic bromine (Br), while photoreduction of Hg^{II} occurs in the aqueous phase as a function of
488 the NO₂ photolysis rate and organic aerosol levels (39). The reduction rate coefficient (K_RED_JNO2)
489 was set to $2.4 \text{ m}^{-3} \mu\text{g}^{-1}$ so that modeled TGM levels agree with observed values in 2005. The Hg

490 chemistry in GEOS-Chem has been updated in more recent model versions (v14 onwards), yet the
491 overall atmospheric lifetime and transport of Hg remain similar (2). Legacy re-emissions of Hg from the
492 ocean are calculated online (depending on temperature and wind speed) through an air-sea exchange
493 parametrization (75), with concentrations of Hg in the surface ocean taken from a previous ocean general
494 circulation model (MITgcm) simulation (39). Soil legacy emissions are parametrized depending on solar
495 radiation, vegetation cover, and concentrations of Hg in soil (76). The model also considers prompt
496 recycling of Hg^{II} deposited to soils and snow (77), geogenic emissions of Hg⁰ (40), and transient
497 emissions of Hg⁰ from biomass burning based on GFED v4.1s (78). More comprehensive descriptions of
498 this version of the GEOS-Chem Hg model can be found elsewhere (39, 70).

499
500 Four simulations (SI Table S3) were performed to evaluate spatial heterogeneity in atmospheric Hg
501 trends under different emissions scenarios (SI Fig. S6), which are intended to be illustrative but do not
502 cover the full range of potential scenarios. The BASE case used Streets et al. (10) anthropogenic
503 emissions of Hg for 2005–2015, with 2016–2020 retaining the same emissions pattern as 2015. The
504 BASE+LEG simulation additionally considered the median box modeled trend (Fig. S5F) in NH legacy
505 emissions (+14 Mg yr⁻²) due to the BASE trend in NH anthropogenic emissions (+23 Mg yr⁻²) over 2005–
506 2020. This trend in legacy emissions was fully ascribed to the ocean through scaling oceanic sea surface
507 concentrations of Hg (39) to yield the NH trend in legacy emissions. To develop a scenario with declining
508 anthropogenic emissions (DEC_ANT) that would be compatible with box model-derived constraints, we
509 scaled South and East Asian emissions in BASE by the trend in Chinese emissions from a national-scale
510 inventory (41, 42) for the years 2005–2017. To extend the emissions to 2020, we extrapolated the linear
511 trend in Chinese emissions from 2013–2017 to 2018–2020. Emissions in regions outside of South and
512 East Asia were kept the same between BASE and DEC_ANT. We also considered the median decline in
513 NH legacy emissions (-1 Mg yr⁻²) due to the decline in NH anthropogenic emissions (-27 Mg yr⁻²) for
514 DEC_ANT, scaling ocean Hg concentrations accordingly. As a fourth scenario, we explored the possibility
515 where anthropogenic emissions follow BASE, but a major decline (-50 Mg yr⁻²) in NH ocean legacy
516 emissions occurs (DEC_LEG_ONLY). Thus, the overall NH emissions decline is similar between
517 DEC_ANT (-33 Mg yr⁻²) and DEC_LEG_ONLY (-30 Mg yr⁻²), but the source contribution and spatial
518 distribution varies. In addition, while DEC_ANT includes stagnant overall SH emissions (-0.5 Mg yr⁻²),
519 DEC_LEG_ONLY has SH emissions declines (-74 Mg yr⁻²) due to the scaling of ocean concentrations.

520 521 **Acknowledgments**

522 This work was funded by the Swiss National Science Foundation through an Early Postdoc.Mobility grant
523 to A.F. (P2EZP2_195424) and a grant (#1924148) from the US National Science Foundation to N.E.S.
524 The EPA through its Office of Research and Development partially funded and contributed to this
525 research. The views expressed in this paper are those of the authors and do not necessarily reflect the
526 views or policies of EPA. It has been subjected to Agency review and approved for publication. Mention of
527 trade names or commercial products do not constitute an endorsement or recommendation for use. The
528 authors acknowledge Environment and Climate Change Canada, Atmospheric Mercury Network (AMNet),
529 New York State Department of Environmental Conservation, European Monitoring and Evaluation
530 Programme (EMEP), Global Mercury Observation System (GMOS), Ministry of Environment Japan
531 (MOEJ), Ministry of Environment (MOENV) Taiwan, and IISD Experimental Lakes Area for the provision
532 of total gaseous mercury data. The authors would like to acknowledge the following for the funding of the
533 Auchencorth Moss UK site, the UK Department for Environment, Food and Rural Affairs (Defra) and the
534 devolved administrations, via the UK Eutrophying and Acidifying Atmospheric Pollutants (UKEAP)
535 contract and by the Natural Environmental Research Council (NERC) National Capability UK-SCaPE
536 programme. K.-L.C. is supported by NOAA cooperative agreement NA22OAR4320151. We would like to
537 thank David Gay and Ralf Ebinghaus for helpful discussion about available Hg measurements.

538

539 **Code and Data Availability**

540 Model code, analysis scripts, simulation data, and processed data to reproduce all figures are published
 541 in Zenodo (<https://doi.org/10.5281/zenodo.10551590>) under a CC BY 4.0 license
 542 (<https://creativecommons.org/licenses/by/4.0/>). The full timeseries of observational data are available
 543 online from AMNet (<https://nadp.slh.wisc.edu/networks/atmospheric-mercury-network/>), CAPMoN,
 544 ([https://www.canada.ca/en/environment-climate-change/services/air-pollution/monitoring-networks-](https://www.canada.ca/en/environment-climate-change/services/air-pollution/monitoring-networks-data/canadian-air-precipitation.html)
 545 [data/canadian-air-precipitation.html](https://www.canada.ca/en/environment-climate-change/services/air-pollution/monitoring-networks-data/canadian-air-precipitation.html)), EMEP (<https://ebas-data.nilu.no>), and GMOS
 546 (<https://sdi.iia.cnr.it/gos4mcat>). EPA Mauna Loa data related to this manuscript can be found at
 547 <https://catalog.data.gov/dataset/epa-sciencehub>. All other observational data are available upon request
 548 to the corresponding measurement network PIs.

549

550 **References**

- 551 1. UNTC, Minamata Convention on Mercury (2013).
 552 2. V. Shah, *et al.*, Improved Mechanistic Model of the Atmospheric Redox Chemistry of Mercury.
 553 *Environ. Sci. Technol.* **55**, 14445–14456 (2021).
 554 3. UNEP/MC/COP.3, “Proposed indicators for evaluating the effectiveness of the Minamata
 555 Convention, by article. Annex I to decision MC-3/10.” (2020).
 556 4. F. Steenhuisen, S. J. Wilson, Development and application of an updated geospatial distribution
 557 model for gridding 2015 global mercury emissions. *Atmos. Environ.* **211**, 138–150 (2019).
 558 5. UNEP, *Global Mercury Assessment 2018* (UN Environment Programme, Chemicals and Health
 559 Branch. Geneva, Switzerland, 2019).
 560 6. H. M. Amos, D. J. Jacob, D. G. Streets, E. M. Sunderland, Legacy impacts of all-time anthropogenic
 561 emissions on the global mercury cycle. *Global Biogeochem. Cycles* **27**, 410–421 (2013).
 562 7. Y. Zhang, *et al.*, Observed decrease in atmospheric mercury explained by global decline in
 563 anthropogenic emissions. *Proc. Natl. Acad. Sci. U.S.A.* **113**, 526–531 (2016).
 564 8. K.-L. Chang, *et al.*, Trend detection of atmospheric time series. *Elementa: Science of the*
 565 *Anthropocene* **9**, 00035 (2021).
 566 9. M. Muntean, *et al.*, Evaluating EDGARv4.tox2 speciated mercury emissions ex-post scenarios and
 567 their impacts on modelled global and regional wet deposition patterns. *Atmospheric Environment*
 568 **184**, 56–68 (2018).
 569 10. D. G. Streets, *et al.*, Global and regional trends in mercury emissions and concentrations, 2010–
 570 2015. *Atmospheric Environment* **201**, 417–427 (2019).
 571 11. D. Custódio, *et al.*, Odds and ends of atmospheric mercury in Europe and over the North Atlantic
 572 Ocean: temporal trends of 25 years of measurements. *Atmos. Chem. Phys.* **22**, 3827–3840 (2022).
 573 12. K. MacSween, *et al.*, Updated trends for atmospheric mercury in the Arctic: 1995–2018. *Science of*
 574 *The Total Environment* **837**, 155802 (2022).
 575 13. C. I. Olson, H. Fakhraei, C. T. Driscoll, Mercury Emissions, Atmospheric Concentrations, and Wet
 576 Deposition across the Conterminous United States: Changes over 20 Years of Monitoring. *Environ.*
 577 *Sci. Technol. Lett.* **7**, 376–381 (2020).
 578 14. K. Marumoto, *et al.*, Long-Term Observation of Atmospheric Speciated Mercury during 2007–2018
 579 at Cape Hedo, Okinawa, Japan. *Atmosphere* **10**, 362 (2019).
 580 15. L. S. P. Nguyen, G.-R. Sheu, D.-W. Lin, N.-H. Lin, Temporal changes in atmospheric mercury
 581 concentrations at a background mountain site downwind of the East Asia continent in 2006–2016.
 582 *Science of The Total Environment* **686**, 1049–1056 (2019).
 583 16. J. Shi, *et al.*, Measurement report: Atmospheric mercury in a coastal city of Southeast China – inter-
 584 annual variations and influencing factors. *Atmos. Chem. Phys.* **22**, 11187–11202 (2022).
 585 17. Q. Wu, *et al.*, Developing a statistical model to explain the observed decline of atmospheric
 586 mercury. *Atmospheric Environment* **243**, 117868 (2020).
 587 18. F. Slemr, *et al.*, Atmospheric mercury in the Southern Hemisphere – Part 1: Trend and inter-annual
 588 variations in atmospheric mercury at Cape Point, South Africa, in 2007–2017, and on Amsterdam
 589 Island in 2012–2017. *Atmos. Chem. Phys.* **20**, 7683–7692 (2020).
 590 19. M. Jiskra, *et al.*, A vegetation control on seasonal variations in global atmospheric mercury
 591 concentrations. *Nature Geosci* **11**, 244–250 (2018).

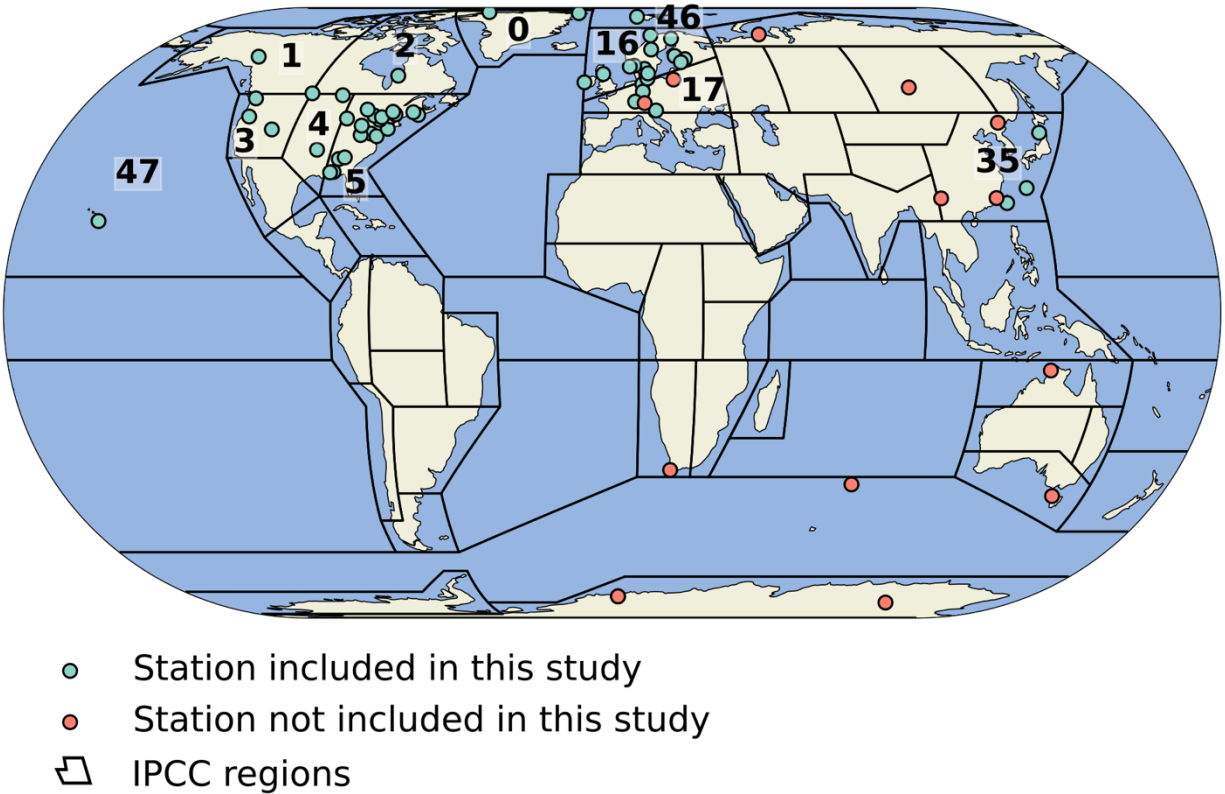
- 592 20. F. Slemr, E.-G. Brunke, R. Ebinghaus, J. Kuss, Worldwide trend of atmospheric mercury since
593 1995. *Atmos. Chem. Phys.* **11**, 4779–4787 (2011).
- 594 21. A. L. Soerensen, *et al.*, Multi-decadal decline of mercury in the North Atlantic atmosphere explained
595 by changing subsurface seawater concentrations. *Geophys. Res. Lett.* **39**, n/a-n/a (2012).
- 596 22. H. Angot, *et al.*, Global and Local Impacts of Delayed Mercury Mitigation Efforts. *Environ. Sci.*
597 *Technol.* **52**, 12968–12977 (2018).
- 598 23. S. N. Lyman, L. E. Gratz, S. M. Dunham-Cheatham, M. S. Gustin, A. Luippold, Improvements to the
599 Accuracy of Atmospheric Oxidized Mercury Measurements. *Environ. Sci. Technol.* **54**, 13379–
600 13388 (2020).
- 601 24. A. Giang, *et al.*, Understanding factors influencing the detection of mercury policies in modelled
602 Laurentian Great Lakes wet deposition. *Environ. Sci.: Processes Impacts* **20**, 1373–1389 (2018).
- 603 25. M. Iturbide, *et al.*, An update of IPCC climate reference regions for subcontinental analysis of
604 climate model data: definition and aggregated datasets. *Earth Syst. Sci. Data* **12**, 2959–2970
605 (2020).
- 606 26. Y. Tang, *et al.*, Recent decrease trend of atmospheric mercury concentrations in East China: the
607 influence of anthropogenic emissions. *Atmos. Chem. Phys.* **18**, 8279–8291 (2018).
- 608 27. P. Sun, *et al.*, Declines of gaseous element mercury concentrations at an urban site in eastern
609 China caused by reductions of anthropogenic emission. *Atmospheric Environment* **317**, 120199
610 (2024).
- 611 28. H. Selin, N. E. Selin, From Stockholm to Minamata and beyond: Governing mercury pollution for a
612 more sustainable future. *One Earth* **5**, 1109–1125 (2022).
- 613 29. D. G. Streets, *et al.*, Five hundred years of anthropogenic mercury: spatial and temporal release
614 profiles. *Environ. Res. Lett.* **14**, 084004 (2019).
- 615 30. D. S. Stevenson, *et al.*, Trends in global tropospheric hydroxyl radical and methane lifetime since
616 1850 from AerChemMIP. *Atmos. Chem. Phys.* **20**, 12905–12920 (2020).
- 617 31. T. S. Dibble, H. L. Tetu, Y. Jiao, C. P. Thackray, D. J. Jacob, Modeling the OH-Initiated Oxidation of
618 Mercury in the Global Atmosphere without Violating Physical Laws. *J. Phys. Chem. A* **124**, 444–453
619 (2020).
- 620 32. J. P. Parrella, *et al.*, Tropospheric bromine chemistry: implications for present and pre-industrial
621 ozone and mercury. *Atmos. Chem. Phys.* **12**, 6723–6740 (2012).
- 622 33. A. Saiz-Lopez, *et al.*, Photochemistry of oxidized Hg(I) and Hg(II) species suggests missing mercury
623 oxidation in the troposphere. *Proc. Natl. Acad. Sci. U.S.A.* **117**, 30949–30956 (2020).
- 624 34. A. Cole, *et al.*, A Survey of Mercury in Air and Precipitation across Canada: Patterns and Trends.
625 *Atmosphere* **5**, 635–668 (2014).
- 626 35. K. Schaefer, *et al.*, Potential impacts of mercury released from thawing permafrost. *Nat Commun*
627 **11**, 4650 (2020).
- 628 36. Y. Wang, P. Wu, Y. Zhang, Climate-driven changes of global marine mercury cycles in 2100. *Proc.*
629 *Natl. Acad. Sci. U.S.A.* **120**, e2202488120 (2023).
- 630 37. B. P. DiMento, R. P. Mason, S. Brooks, C. Moore, The impact of sea ice on the air-sea exchange of
631 mercury in the Arctic Ocean. *Deep Sea Research Part I: Oceanographic Research Papers* **144**, 28–
632 38 (2019).
- 633 38. A. Kumar, S. Wu, Y. Huang, H. Liao, J. O. Kaplan, Mercury from wildfires: Global emission
634 inventories and sensitivity to 2000–2050 global change. *Atmospheric Environment* **173**, 6–15
635 (2018).
- 636 39. H. M. Horowitz, *et al.*, A new mechanism for atmospheric mercury redox chemistry: implications for
637 the global mercury budget. *Atmos. Chem. Phys.* **17**, 6353–6371 (2017).
- 638 40. N. E. Selin, *et al.*, Chemical cycling and deposition of atmospheric mercury: Global constraints from
639 observations. *J. Geophys. Res.* **112**, D02308 (2007).
- 640 41. K. Liu, *et al.*, Measure-Specific Effectiveness of Air Pollution Control on China’s Atmospheric
641 Mercury Concentration and Deposition during 2013–2017. *Environ. Sci. Technol.* **53**, 8938–8946
642 (2019).
- 643 42. Q. Wu, *et al.*, Temporal Trend and Spatial Distribution of Speciated Atmospheric Mercury Emissions
644 in China During 1978–2014. *Environ. Sci. Technol.* **50**, 13428–13435 (2016).
- 645 43. Å. Iverfeldt, J. Munthe, C. Brosset, J. Pacyna, “Long-Term Changes in Concentration and
646 Deposition of Atmospheric Mercury Over Scandinavia” in *Mercury as a Global Pollutant:*
647 *Proceedings of the Third International Conference Held in Whistler, British Columbia, July 10–14,*

- 648 1994, D. B. Porcella, J. W. Huckabee, B. Wheatley, Eds. (Springer Netherlands, 1995), pp. 227–
649 233.
- 650 44. F. Slemr, H. E. Scheel, Trends in atmospheric mercury concentrations at the summit of the Wank
651 mountain, southern Germany. *Atmospheric Environment* **32**, 845–853 (1998).
- 652 45. Y. Zhang, *et al.*, Improved Anthropogenic Mercury Emission Inventories for China from 1980 to
653 2020: Toward More Accurate Effectiveness Evaluation for the Minamata Convention. *Environ. Sci.*
654 *Technol.* **57**, 8660–8670 (2023).
- 655 46. M. Muntean, *et al.*, Trend analysis from 1970 to 2008 and model evaluation of EDGARv4 global
656 gridded anthropogenic mercury emissions. *Science of The Total Environment* **494–495**, 337–350
657 (2014).
- 658 47. H. M. Horowitz, D. J. Jacob, H. M. Amos, D. G. Streets, E. M. Sunderland, Historical Mercury
659 Releases from Commercial Products: Global Environmental Implications. *Environ. Sci. Technol.* **48**,
660 10242–10250 (2014).
- 661 48. S. Y. Kwon, *et al.*, Mercury stable isotopes for monitoring the effectiveness of the Minamata
662 Convention on Mercury. *Earth-Science Reviews* **203**, 103111 (2020).
- 663 49. J. A. Fisher, *et al.*, A synthesis of mercury research in the Southern Hemisphere, part 2:
664 Anthropogenic perturbations. *Ambio* **52**, 918–937 (2023).
- 665 50. L. Schneider, *et al.*, A synthesis of mercury research in the Southern Hemisphere, part 1: Natural
666 processes. *Ambio* **52**, 897–917 (2023).
- 667 51. D. S. McLagan, *et al.*, A High-Precision Passive Air Sampler for Gaseous Mercury. *Environ. Sci.*
668 *Technol. Lett.* **3**, 24–29 (2016).
- 669 52. F. De Simone, *et al.*, A Chemical Transport Model Emulator for the Interactive Evaluation of Mercury
670 Emission Reduction Scenarios. *Atmosphere* **11**, 878 (2020).
- 671 53. C. W. Tessum, J. D. Hill, J. D. Marshall, InMAP: A model for air pollution interventions. *PLoS ONE*
672 **12**, e0176131 (2017).
- 673 54. W. Atkinson, *et al.*, A tool for air pollution scenarios (TAPS v1.0) to enable global, long-term, and
674 flexible study of climate and air quality policies. *Geosci. Model Dev.* **15**, 7767–7789 (2022).
- 675 55. P. J. Blanchfield, *et al.*, Experimental evidence for recovery of mercury-contaminated fish
676 populations. *Nature* **601**, 74–78 (2022).
- 677 56. D. A. Gay, *et al.*, The Atmospheric Mercury Network: measurement and initial examination of an
678 ongoing atmospheric mercury record across North America. *Atmos. Chem. Phys.* **13**, 11339–11349
679 (2013).
- 680 57. K. Tørseth, *et al.*, Introduction to the European Monitoring and Evaluation Programme (EMEP) and
681 observed atmospheric composition change during 1972–2009. *Atmos. Chem. Phys.* **12**, 5447–5481
682 (2012).
- 683 58. F. Sprovieri, *et al.*, Atmospheric mercury concentrations observed at ground-based monitoring sites
684 globally distributed in the framework of the GMOS network. *Atmos. Chem. Phys.* **16**, 11915–11935
685 (2016).
- 686 59. V. L. St. Louis, *et al.*, Atmospheric Concentrations and Wet/Dry Loadings of Mercury at the Remote
687 Experimental Lakes Area, Northwestern Ontario, Canada. *Environ. Sci. Technol.* **53**, 8017–8026
688 (2019).
- 689 60. F. Carbone, *et al.*, Sea surface temperature variation linked to elemental mercury concentrations
690 measured on Mauna Loa. *Geophys. Res. Lett.* **43**, 7751–7757 (2016).
- 691 61. M. S. Landis, R. K. Stevens, F. Schaedlich, E. M. Prestbo, Development and Characterization of an
692 Annular Denuder Methodology for the Measurement of Divalent Inorganic Reactive Gaseous
693 Mercury in Ambient Air. *Environ. Sci. Technol.* **36**, 3000–3009 (2002).
- 694 62. S. Sholupov, S. Pogarev, V. Ryzhov, N. Mashyanov, A. Stroganov, Zeeman atomic absorption
695 spectrometer RA-915+ for direct determination of mercury in air and complex matrix samples. *Fuel*
696 *Processing Technology* **85**, 473–485 (2004).
- 697 63. Å. Iverfeldt, Occurrence and turnover of atmospheric mercury over the nordic countries. *Water, Air,*
698 *and Soil Pollution* **56**, 251–265 (1991).
- 699 64. K.-L. Chang, M. G. Schultz, G. Koren, Selke, Niklas, Guidance note on best statistical practices for
700 TOAR analyses. Available at: <https://doi.org/10.48550/arXiv.2304.14236> (2023).
- 701 65. D. Bates, M. Mächler, B. Bolker, S. Walker, Fitting Linear Mixed-Effects Models Using *lme4*. *J. Stat.*
702 *Soft.* **67** (2015).

- 703 66. R. Koenker, K. F. Hallock, Quantile Regression. *The Journal of Economic Perspectives* **15**, 143–
704 156 (2001).
- 705 67. K.-L. Chang, *et al.*, Impact of the COVID-19 Economic Downturn on Tropospheric Ozone Trends:
706 An Uncertainty Weighted Data Synthesis for Quantifying Regional Anomalies Above Western North
707 America and Europe. *AGU Advances* **3**, e2021AV000542 (2022).
- 708 68. W. C. Porter, C. L. Heald, D. Cooley, B. Russell, Investigating the observed sensitivities of air-
709 quality extremes to meteorological drivers via quantile regression. *Atmos. Chem. Phys.* **15**, 10349–
710 10366 (2015).
- 711 69. R. Koenker, quantreg: Quantile Regression. Available at: [https://CRAN.R-](https://CRAN.R-project.org/package=quantreg)
712 [project.org/package=quantreg](https://CRAN.R-project.org/package=quantreg) (2022).
- 713 70. A. Feinberg, T. Dlamini, M. Jiskra, V. Shah, N. E. Selin, Evaluating atmospheric mercury (Hg)
714 uptake by vegetation in a chemistry-transport model. *Environ. Sci.: Processes Impacts* **24**, 1303–
715 1318 (2022).
- 716 71. M. D. McKay, R. J. Beckman, W. J. Conover, Comparison of Three Methods for Selecting Values of
717 Input Variables in the Analysis of Output from a Computer Code. *Technometrics* **21**, 239–245
718 (1979).
- 719 72. N. E. Selin, A proposed global metric to aid mercury pollution policy. *Science* **360**, 607–609 (2018).
- 720 73. H. M. Amos, *et al.*, Global Biogeochemical Implications of Mercury Discharges from Rivers and
721 Sediment Burial. *Environ. Sci. Technol.* **48**, 9514–9522 (2014).
- 722 74. R. Gelaro, *et al.*, The Modern-Era Retrospective Analysis for Research and Applications, Version 2
723 (MERRA-2). *J. Clim.* **30**, 5419–5454 (2017).
- 724 75. P. D. Nightingale, *et al.*, In situ evaluation of air-sea gas exchange parameterizations using novel
725 conservative and volatile tracers. *Global Biogeochem. Cycles* **14**, 373–387 (2000).
- 726 76. S. Song, *et al.*, Top-down constraints on atmospheric mercury emissions and implications for global
727 biogeochemical cycling. *Atmos. Chem. Phys.* **15**, 7103–7125 (2015).
- 728 77. N. E. Selin, *et al.*, Global 3-D land-ocean-atmosphere model for mercury: Present-day versus
729 preindustrial cycles and anthropogenic enrichment factors for deposition. *Global Biogeochem.*
730 *Cycles* **22**, GB2011 (2008).
- 731 78. G. R. van der Werf, *et al.*, Global fire emissions estimates during 1997–2016. *Earth Syst. Sci. Data*
732 **9**, 697–720 (2017).

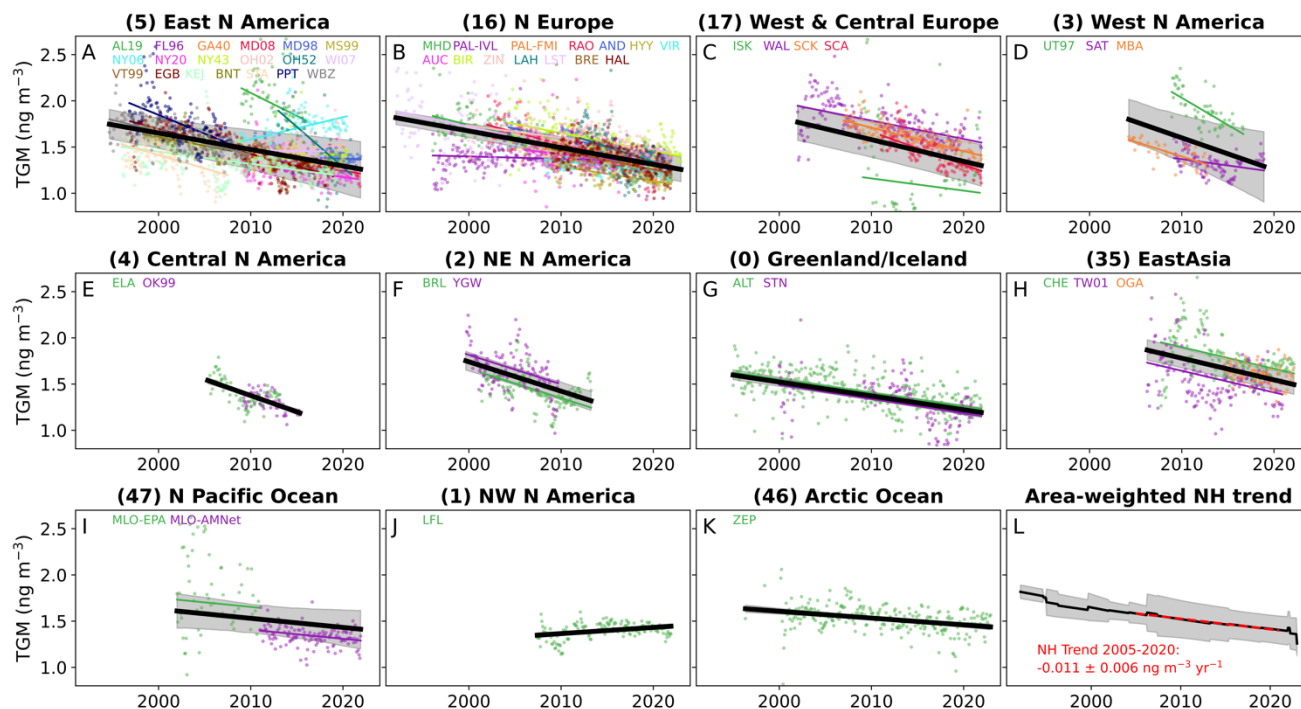
733
734

735 **Figures**



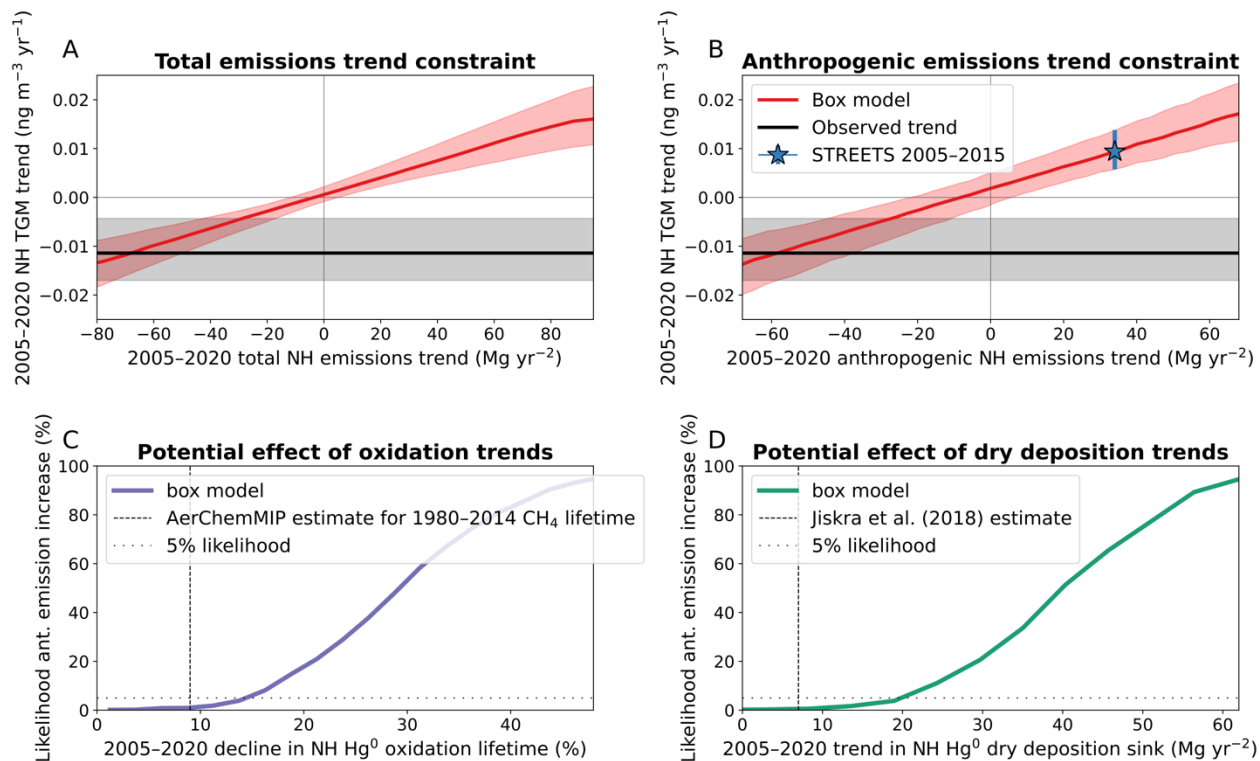
736
737
738
739
740
741

Figure 1. Map of observation stations that measured atmospheric Hg concentrations for more than 6 years (Table S1). Defined regions (25) are indicated with black lines, with corresponding numbering of included regions listed on the map. For this study, we included NH stations with openly accessible or provided datasets.

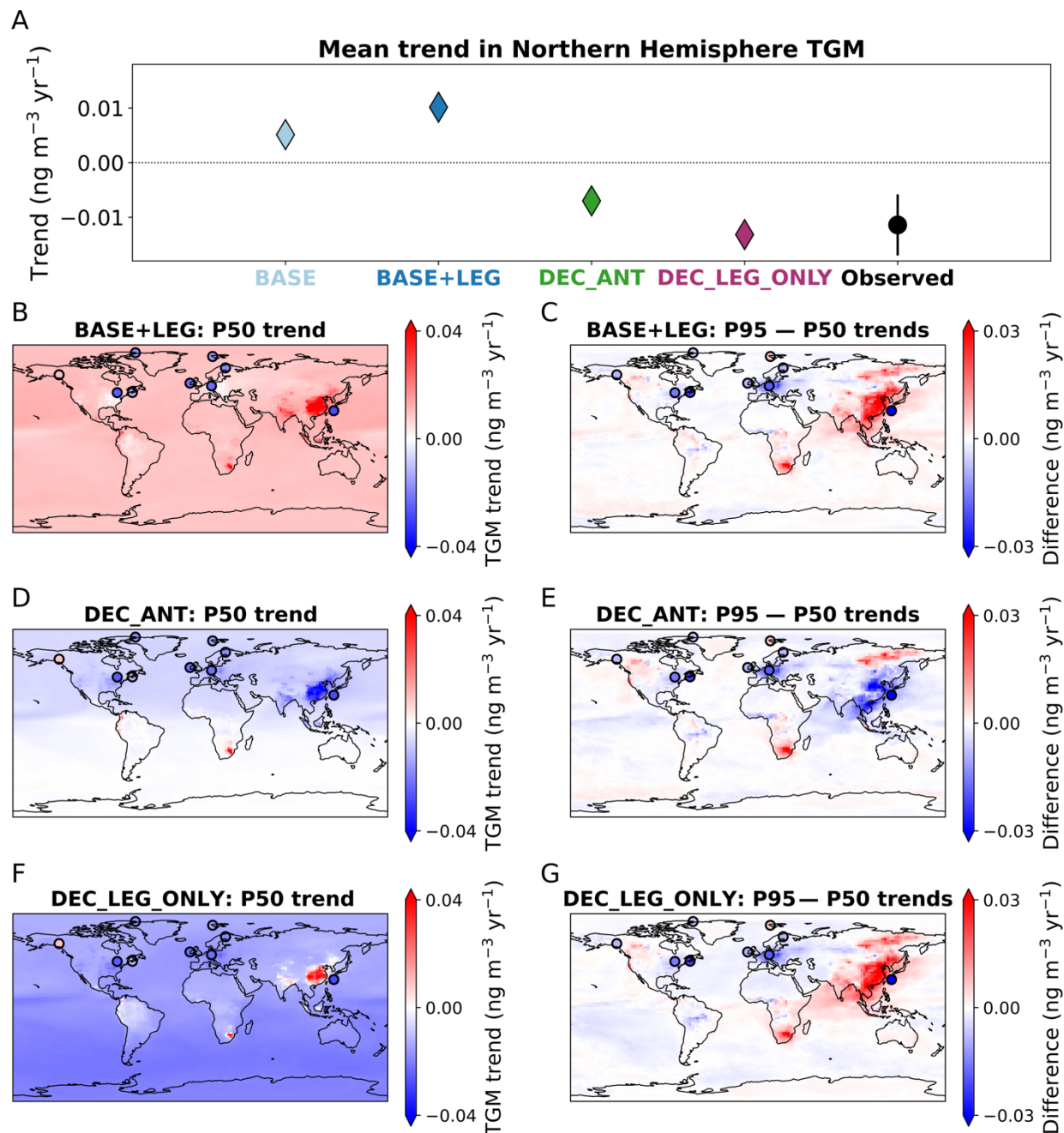


742
 743 **Figure 2.** Trends in observed total gaseous mercury (TGM), aggregated by the regions (A–K) in Fig. 1
 744 (labelled by region number). Trends are calculated with linear mixed effects modeling, with overall
 745 regional trends shown in black and shading shows the 5th to 95th percentile range. Individual site
 746 deseasonalized monthly means are shown as colored points and individual regressions as colored lines.
 747 The overall Northern Hemisphere (NH) trend (L) is calculated by taking the area-weighted average of
 748 regional trends, with the shading showing the 2 σ averaging error. The red dashed curve in L is the linear
 749 regression trend for 2005–2020, with trend error representing 2 σ error from resampling regional trends
 750 within their error bounds. We distinguished data from sites where measurements were made by multiple
 751 networks, i.e., Pallas (FMI and IVL) and Mauna Loa (EPA and AMNet).

752
 753



754
 755 **Figure 3.** Modeled relationships between 2005–2020 trends in NH Total Gaseous Mercury (TGM)
 756 concentrations and drivers. (A) Relationship between NH TGM trends and the trends in total NH
 757 emissions. The 10⁵ box model simulations are summarized in the red line (median) and shading (5th to
 758 95th percentile). Observed NH TGM trends are shown in the horizontal black line, with the associated
 759 error shaded. The overlap between black and red shading represents the parameter space where the
 760 model is compatible with observed trends. (B) Relationship between NH TGM trends and trends in
 761 anthropogenic NH emissions. The Streets et al. (10) trend is plotted as a blue star marker, with error
 762 showing the predicted box model range for the NH TGM trend. (C) Impact of NH Hg⁰ oxidation lifetime
 763 trends on the likelihood of positive anthropogenic (ant.) trends for 2005–2020. The y-axis refers to the
 764 percent of box model runs fitting with the observed NH TGM trend ($\pm 2\sigma$) that have positive anthropogenic
 765 emissions trends. The AerChemMIP (30) estimate for the 1980–2014 methane (CH₄) oxidation lifetime is
 766 shown for context. (D) Impact of NH Hg⁰ dry deposition sink on the likelihood of positive anthropogenic
 767 (ant.) trends for 2005–2020. The estimated trend in NH dry deposition from Jiskra et al. (19) is shown for
 768 context.
 769



770
 771 **Figure 4.** Comparison between trends (2005–2020) in GEOS-Chem model simulations and observations
 772 for Northern Hemisphere (NH) mean TGM (A), calculated using linear mixed effects modeling of available
 773 NH regions and calculating the area-weighted mean (Fig. 2). Error bars refer to the 2σ error but are
 774 smaller than markers for the model simulations. Trend in median (P50) daily deseasonalized simulated
 775 values in BASE+LEG (B), DEC_ANT (D), and DEC_LEG_ONLY (F) for each model grid cell. Observed
 776 results are plotted in filled circles for 9 stations with more than 13 years of high frequency data.
 777 Differences between 95th percentile (P95) trend and median (P50) trend shown for BASE+LEG (C),
 778 DEC_ANT (E), and DEC_LEG_ONLY (G) simulations and observations.

1 **Supplementary Information (SI) for**

2 Increasing anthropogenic emissions inconsistent with declining atmospheric mercury
3 concentrations

4 Aryeh Feinberg^{a*}, Noelle E. Selin^{a,b}, Christine F. Braban^c, Kai-Lan Chang^{d,e}, Danilo Custódio^f, Daniel A.
5 Jaffe^{g,h}, Katriina Kyllönenⁱ, Matthew S. Landis^j, Sarah R. Leeson^c, Koketso M. Molepo^k, Marijana
6 Murovec^l, Michelle G. Nerentorp Mastromonaco^m, Katrine Aspmo Pfaffhuberⁿ, Julian Rüdiger^o, Guey-
7 Rong Sheu^p, and Vincent L. St.Louis^q

8 ^a *Institute for Data, Systems, and Society, Massachusetts Institute of Technology, Cambridge, MA 02139,*
9 *USA*

10 ^b *Department of Earth, Atmospheric, and Planetary Sciences, Massachusetts Institute of Technology,*
11 *Cambridge, MA 02139, USA*

12 ^c *UK Centre for Ecology & Hydrology (UKCEH), Penicuik, Midlothian EH26 0QB, UK*

13 ^d *Cooperative Institute for Research in Environmental Sciences, University of Colorado, Boulder, CO*
14 *80309-0401, USA*

15 ^e *NOAA Chemical Sciences Laboratory, Boulder, CO 80305, USA*

16 ^f *Max-Planck-Institut für Biogeochemie, D-07745 Jena, Germany*

17 ^g *School of STEM, University of Washington Bothell, Bothell, WA 98011, USA*

18 ^h *Department of Atmospheric Sciences, University of Washington Seattle, Seattle, WA 98195, USA*

19 ⁱ *Finnish Meteorological Institute, Helsinki 00560, Finland*

20 ^j *United States Environmental Protection Agency, Office of Research and Development, Research*
21 *Triangle Park, NC 27711, USA*

22 ^k *Institute of Coastal Environmental Chemistry, Helmholtz Zentrum Hereon, 21502 Geesthacht, Germany*

23 ^l *Slovenian Environment Agency, Environment and Nature protection Office, Air Quality Division, 1000*
24 *Ljubljana, Slovenia*

25 ^m *IVL Swedish Environmental Research Institute, SE-411 33 Gothenburg, Sweden*

26 ⁿ *NILU, 2027 Kjeller, Norway*

27 ^o *Air Monitoring Network, German Environment Agency, 63225 Langen, Germany*

28 ^p *Department of Atmospheric Sciences, National Central University, Taoyuan 320, Taiwan*

29 ^q *Department of Biological Sciences, University of Alberta, Edmonton, AB T6G 2E9, Canada*

30 *Correspondence to: arifeinberg@gmail.com (A.F.)

31

32 **This PDF file includes:**

33 Supplementary Text

34 Figures S1 to S7

35 Tables S1 to S3

36 Supplementary References

37 **Section S1. Observation station information**

38 Table S1. List of sites measuring total gaseous mercury (TGM) included in this study.

Site code	Location	Latitude	Longitude	Measurement Network	IPCC Region ^a	Years available
AL19	Birmingham, USA	33.6	-86.8	AMNet ^b	5	2009–2015
FL96	Pensacola, USA	30.5	-87.4	AMNet ^b	5	2009–2015
GA40	Yorkville, USA	33.9	-85.0	AMNet ^b	5	2009–2015
MD08	Piney Reservoir, USA	39.7	-79.0	AMNet ^b	5	2009–2021
MD98	Beltsville, USA	39.0	-76.8	AMNet ^b	5	2009–2021
MS99	Grand Bay, USA	30.4	-88.4	AMNet ^b	5	2009–2020
NY06	Bronx, USA	40.9	-73.9	AMNet ^b	5	2008–2020
NY20	Huntington Forest, USA	44.0	-74.2	AMNet ^b	5	2009–2021
NY43	Rochester, USA	43.1	-77.5	AMNet ^b	5	2008–2020
OH02	Athens, USA	39.3	-82.1	AMNet ^b	5	2009–2020
OH52	South Bass Island, USA	41.7	-82.8	AMNet ^b	5	2013–2020
OK99	Stillwell, USA	35.8	-94.7	AMNet ^b	4	2009–2015
UT97	Salt Lake City, USA	40.7	-112.0	AMNet ^b	3	2008–2017
VT99	Underhill, USA	44.5	-72.9	AMNet ^b	5	2009–2016
WI07	Horicon Marsh, USA	43.5	-88.6	AMNet ^b	5	2011–2017
MLO	Mauna Loa, USA	19.5	-155.6	AMNet ^b /EPA ^c /NOAA	47	2002–2021
MBA	Mt. Bachelor, USA	44.0	-121.7	GMOS ^d	3	2004–2012
ALT	Alert, Canada	82.5	-62.3	CAPMoN ^e	0	1995–2021
BNT	Burnt Island, Canada	45.8	-82.9	CAPMoN ^e	5	1998–2007
BRL	Bratt's Lake, Canada	50.2	-104.7	CAPMoN ^e	2	2001–2013
EGB	Egbert, Canada	44.2	-79.8	CAPMoN ^e	5	1996–2018
KEJ	Kejimikujik, Canada	44.4	-65.2	AMNet ^b /CAPMoN ^e	5	1996–2018
LFL	Little Fox Lake, Canada	61.4	-135.6	CAPMoN ^e	1	2007–2021
PPT	Point Petre, Canada	43.8	-77.1	CAPMoN ^e	5	1996–2007
SAT	Saturna, Canada	48.8	-123.2	CAPMoN ^e	3	2009–2018
STA	Huntsman Science Centre, Canada	45.1	-67.1	CAPMoN ^e	5	1995–2007
WBZ	St. Anicet, Canada	45.1	-74.3	CAPMoN ^e	5	1994–2009
YGW	Kuujuarapik, Canada	55.3	-77.7	CAPMoN ^e	2	1999–2009
ELA	Experimental Lakes Area, Canada	49.7	-93.7	IISD ^f	4	2005–2013
AND	Andøya, Norway	69.3	16.0	EMEP ^g	16	2004–2021
AUC	Auchencorth Moss, UK	55.8	-3.2	EMEP ^g	16	2006–2022
BIR	Birkenes, Norway	58.4	8.3	EMEP ^g	16	2004–2023
BRE	Bredkålen, Sweden	63.9	15.3	EMEP ^g	16	2009–2021
HAL	Hallahus/Vavihill ^h , Sweden	56.0	13.1	EMEP ^g	16	2009–2021
HYY	Hyytiälä, Finland	61.6	24.0	EMEP ^g	16	2009–2021
ISK	Iskrba, Slovenia	45.6	14.9	EMEP ^g	17	2009–2021
LAH	Lahemaa, Estonia	59.5	25.9	EMEP ^g	16	2012–2021
LST	Lista, Norway	58.1	6.6	EMEP ^g	16	1992–2004
MHD	Mace Head, Ireland	53.3	-9.9	EMEP ^g /GMOS ^d	16	1996–2022
PAL	Pallas, Finland	68.0	24.4	EMEP ^g /GMOS ^d	16	1996–2021
RAO	Råö, Sweden	57.4	11.9	EMEP ^g /GMOS ^d	16	2002–2020
SCA	Schauinsland, Germany	47.9	7.9	EMEP ^g	17	2011–2021
SCK	Schmücke, Germany	50.7	10.8	EMEP ^g	17	2007–2021
STN	Station Nord/Villum, Greenland	81.6	-16.6	EMEP ^g	0	2000–2021
VIR	Virolahti, Finland	60.5	27.7	EMEP ^g	16	2008–2021
WAL	Waldhof, Germany	52.8	10.8	EMEP ^g	17	2002–2021
ZEP	Zeppelin, Norway	78.9	11.9	EMEP ^g	46	1994–2022
ZIN	Zingst, Germany	54.4	12.7	EMEP ^g	16	1999–2021
TW01	Mt. Lulin, Taiwan	23.5	120.9	AMNet ^b / MOENV Taiwan ⁱ	35	2006–2020
CHE	Cape Hedo, Japan	26.9	128.3	MOEJ ^j	35	2007–2022
OGA	Oga Peninsula, Japan	39.9	139.9	MOEJ ^j	35	2014–2022

39 ^a IPCC regions are defined with the numbering in Fig. 1, taken from Iturbide et al. (1) ^b Gay et al. (2)
 40 ^c Carbone et al. (3) ^d Sprovieri et al. (4) ^e Cole et al. (5) ^f St. Louis et al. (6) ^g Tørseth et al. (7)
 41 ^h Site changed location in 2016, but due to nearby locations (<3 km apart), they are combined in this analysis
 42 ⁱ Nguyen et al. (8) ^j Marumoto et al. (9)

43 **Section S2. Trend results by region**44 **Table S2.** Tabulated overall regional trends ($\pm 2\sigma$) calculated through linear mixed effects modelling.

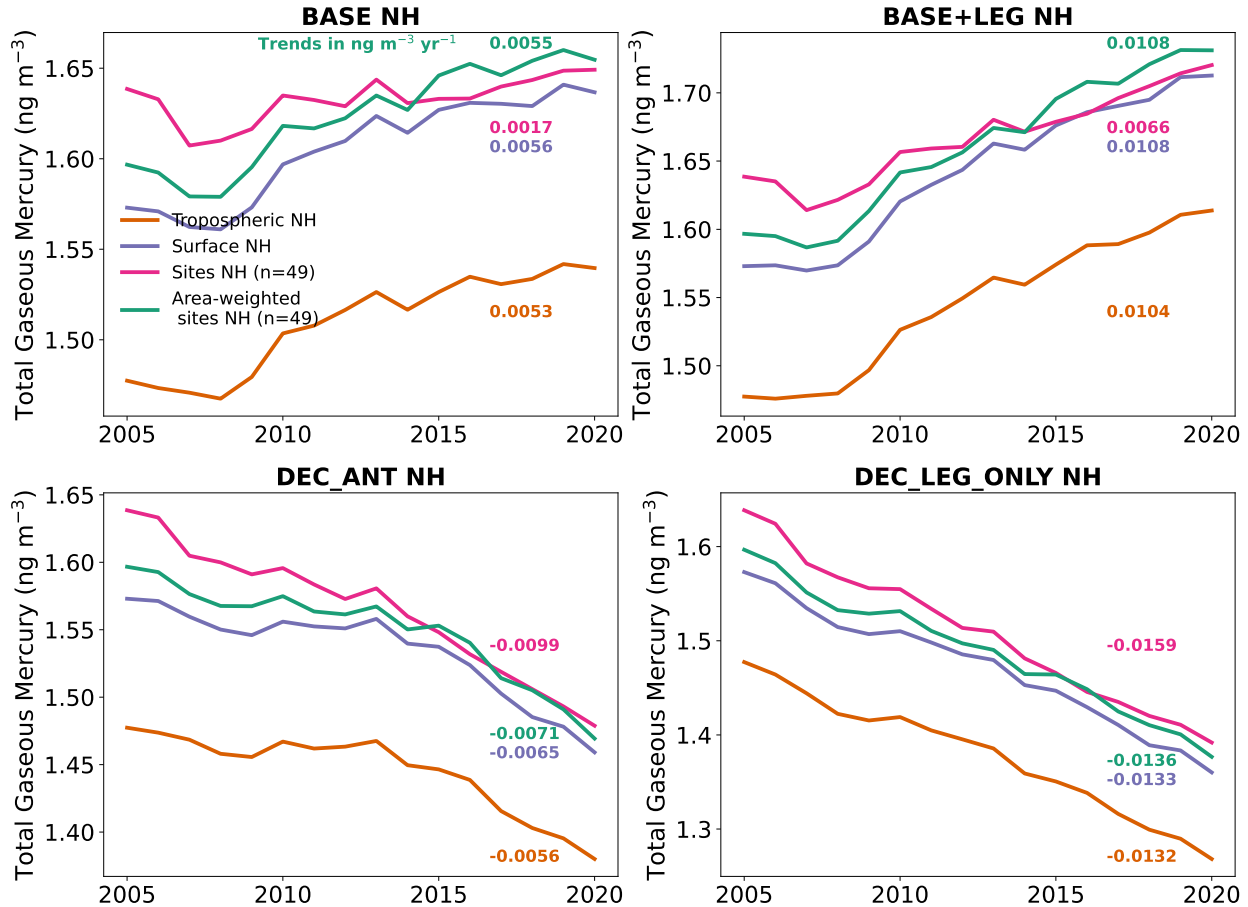
Region name (number)	Number of sites	Area (10^6 km^2)	Trend ($\text{ng m}^{-3} \text{ yr}^{-1}$)
Eastern North America (5)	19	5.69	-0.018 ± 0.012
Northern Europe (16)	13	5.00	-0.018 ± 0.004
West & Central Europe (17)	4	3.79	-0.024 ± 0.010
Western North America (3)	3	3.14	-0.035 ± 0.025
Central North America (4)	2	2.93	-0.035 ± 0.007
Northeastern North America (2)	2	7.66	-0.032 ± 0.009
Greenland/Iceland (0)	2	4.77	-0.015 ± 0.003
East Asia (35)	3	9.46	-0.023 ± 0.005
North Pacific Ocean (47)	1	51.61	-0.010 ± 0.011
Northwestern North America (1)	1	7.51	0.007 ± 0.003
Arctic Ocean (1)	1	6.35	-0.007 ± 0.002
Northern Hemisphere (NH) area-weighted average	51		-0.011 ± 0.006

45

46

47 **Section S3. Sensitivity of trends to statistical approach**48 *Section S3.1 Modelled differences between site, surface, and troposphere NH trends*

49 We used the four GEOS-Chem simulations to test different approaches for calculating overall trends in
50 NH TGM (Fig. S1). We calculated annual averages of the model results over the entire NH troposphere
51 (orange lines), representative of the NH tropospheric box in the 3-box model simulations. We compared
52 this to simulated NH surface TGM concentrations (purple lines), which is the quantity that can actually be
53 measured by surface observation stations. The calculated 2005–2020 trends in surface TGM agree within
54 $0.0005 \text{ ng m}^{-3} \text{ yr}^{-1}$ of tropospheric TGM trends for all simulations except DEC_ANT, where surface
55 declines are faster than tropospheric declines by $0.0009 \text{ ng m}^{-3} \text{ yr}^{-1}$. This can be explained by enhanced
56 dilution of the negative emissions trends when considering the whole troposphere versus the surface
57 level. To approximate the real situation where only a small fraction of the NH surface is measured, we
58 averaged only the model grid cells that contain the 51 observation sites (magenta line in Fig. S1). This
59 approach leads to biases of up to $0.0042 \text{ ng m}^{-3} \text{ yr}^{-1}$ due to the uneven distribution of observation stations
60 (Fig. 1) throughout the NH, with some regions covered more than others and other regions having no
61 observations. This bias can be reduced to below $0.0006 \text{ ng m}^{-3} \text{ yr}^{-1}$ by first averaging by IPCC region the
62 grid cells that correspond to observation sites (Fig. 1) and then calculating an area-weighted average for
63 the NH (green line), similar to what was done for the observation analysis in the main manuscript (Fig. 2).
64 Therefore, it is best to use the approach of area-weighted site averages when limited observation stations
65 are available, leading to good agreement with the surface trends in TGM. We expanded the observed
66 trend uncertainty in Figs. 3A and B upwards by $0.0015 \text{ ng m}^{-3} \text{ yr}^{-1}$ (max error between area-weighted and
67 tropospheric trends, DEC_ANT), due to the potential overestimate of NH tropospheric trends by only
68 having surface observations (Fig. S1).

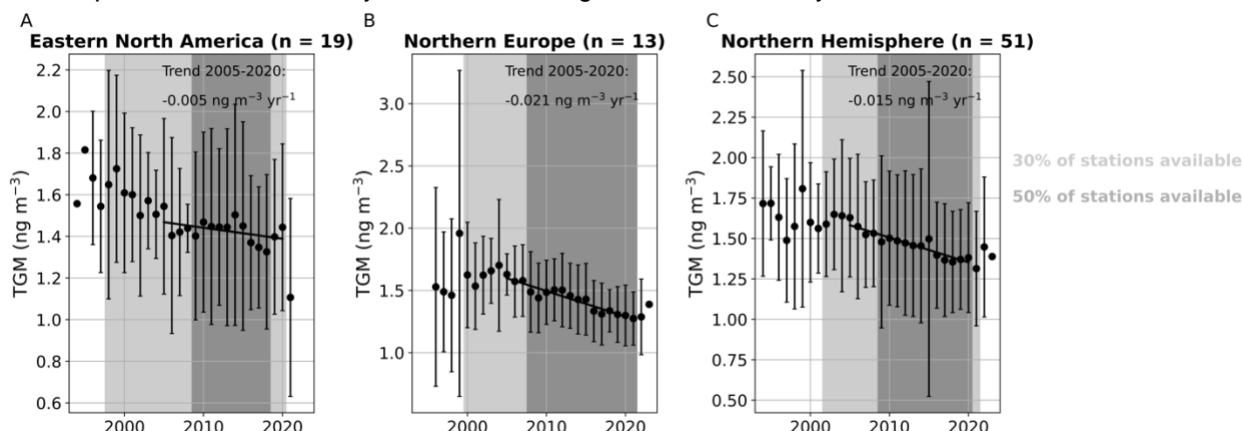


69

70 **Figure S1.** Different methods of calculating hemispheric average trends applied to GEOS-Chem
 71 simulations of total gaseous mercury (TGM). We compared annual mean simulated timeseries of NH
 72 tropospheric averages, NH surface averages, averaging model grid cells where observation sites are
 73 located, and area-weighted averaging of regional averages of model grid cells where observation sites
 74 are located. Linear regression trends over 2005–2020 are listed in units of $\text{ng m}^{-3} \text{yr}^{-1}$.
 75

76 *Section S3.2 Aggregation of observation stations into overall NH annual averages using “bucket” method*
 77 Previous studies (e.g., 10) have calculated overall timeseries for regions by averaging all available
 78 stations for each specific year (“bucket” method). Biases can arise in this approach from multiple sources
 79 of error: 1) sites have individual offsets and trends due to measurement method differences or specific
 80 local sources, leading to biases in a “bucket” average because sites do not all cover the same time
 81 period; 2) sites are unevenly distributed, with certain regions over- or under-represented; and 3) certain
 82 months can be missing in a specific year, which due to the strong seasonality of TGM can bias the annual
 83 mean. We aimed to address these drawbacks in our approach by explicitly modeling offsets between
 84 sites using linear mixed effects models, deseasonalizing monthly means from all observations, and
 85 aggregating results by IPCC regions before calculating area-weighted averages. We applied the bucket
 86 approach to calculate 2005–2020 trends in Eastern North America (19 sites), Northern Europe (13 sites),
 87 and the NH (51 sites) (Fig. S2) to compare with our results in this manuscript. Overall, the derived trends
 88 are similar for the NH between our approach ($-0.011 \pm 0.006 \text{ ng m}^{-3} \text{ yr}^{-1}$) and the “bucket” approach
 89 ($-0.015 \text{ ng m}^{-3} \text{ yr}^{-1}$). Issues with the bucket method were observed for periods when less sites are
 90 available (e.g., before the year 2000 in Fig. S2), which show high variability due to differences in the
 91 number and characteristics of averaged sites for each year. Therefore, we recommend that caution be

92 exercised with such an approach, as the derived aggregated timeseries may be misleading and could be
 93 misinterpreted as real variability rather than changes in site availability.



94
 95 **Figure S2.** “Bucket” method trends calculated by averaging all available station data (not
 96 deseasonalized) for each year for Eastern North America (A), Northern Europe (B), and the overall
 97 Northern Hemisphere (C). Error bars show the 2σ variation in station averages. Shading shows the years
 98 where at least 30% (light gray) and 50% of the stations (dark gray) are available. Linear regression trends
 99 are calculated over 2005–2020 and listed on the plot.

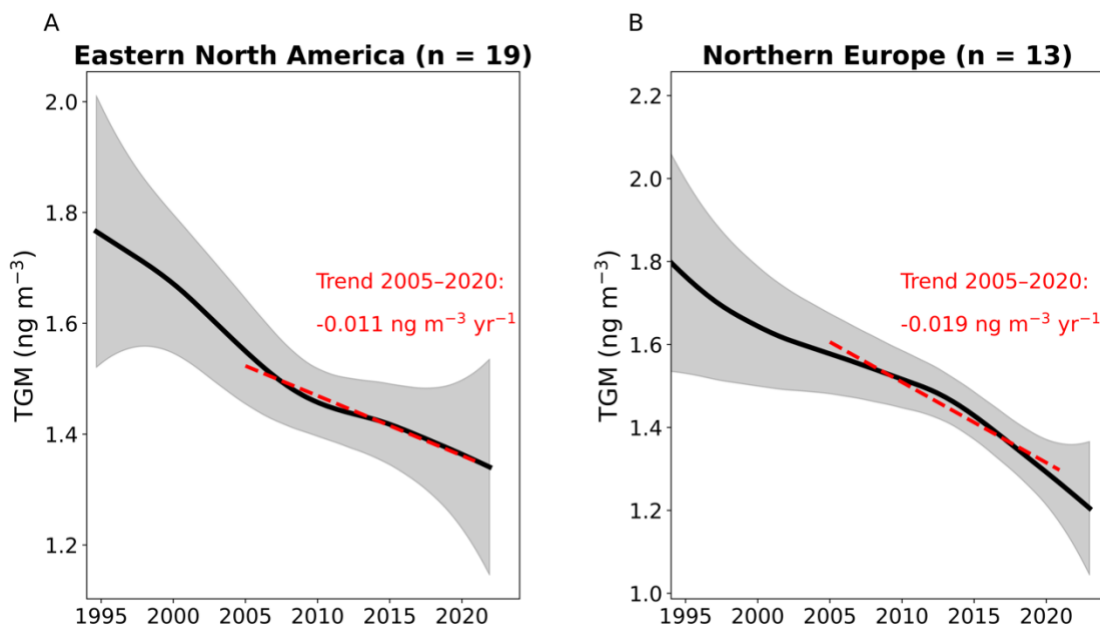
100
 101 *Section S3.3 Using Generalized Additive Models (GAM) to aggregate multisite data*

102 To test the robustness of our regional trend results to other approaches, we applied the approach of
 103 Chang et al. (11) to use Generalized Additive Models (GAM) to aggregate multisite data into an overall
 104 trend. In this regression-based approach, we modeled the deseasonalized TGM monthly mean values at
 105 multiple sites as a function of site (s) and time (t):

$$\text{obs}(s,t) = \text{regional trend}(t) + \text{regional seasonality}(t) + \text{site offset}(s) + \text{site-specific trend}(s,t) + \text{site-specific seasonality}(s,t) + \text{AR}(1) \text{ error} \quad (\text{Eq. S1})$$

111 The GAM approach fits smooth functions of the predictor variables, which include time, month-of-year (for
 112 seasonality), and the categorical site ID (for site-specific terms). We used the implementation of GAM in
 113 the R package mgcv (12) and calculated fits using the restricted maximum likelihood (REML) method to
 114 avoid overfitting.

115 The GAM method is not suitable when only a few sites are available within a region (13), so in the
 116 main manuscript we focused on linear mixed effect models of regional trends. For the GAM analysis here,
 117 we investigated the two regions with more than 10 sites (Eastern North America and Northern Europe).
 118 GAM helped to identify nonlinearities in the overall regional trend, for example, a deceleration in the
 119 Eastern North America TGM decline occurred after ~2009. We analyzed the 2005–2020 linear trend
 120 obtained from the GAM curves for Eastern North America (-0.011 ng m⁻³ yr⁻¹) and Northern Europe
 121 (-0.019 ng m⁻³ yr⁻¹). Since both of these trends are within the error of the results obtained for linear mixed
 122 effects modeling (Eastern North America: -0.018 ± 0.012 ng m⁻³ yr⁻¹; Northern Europe: -0.018 ± 0.004 ng
 123 m⁻³ yr⁻¹), we conclude that the derived regional declines are relatively robust to the choice of statistical
 124 approach.



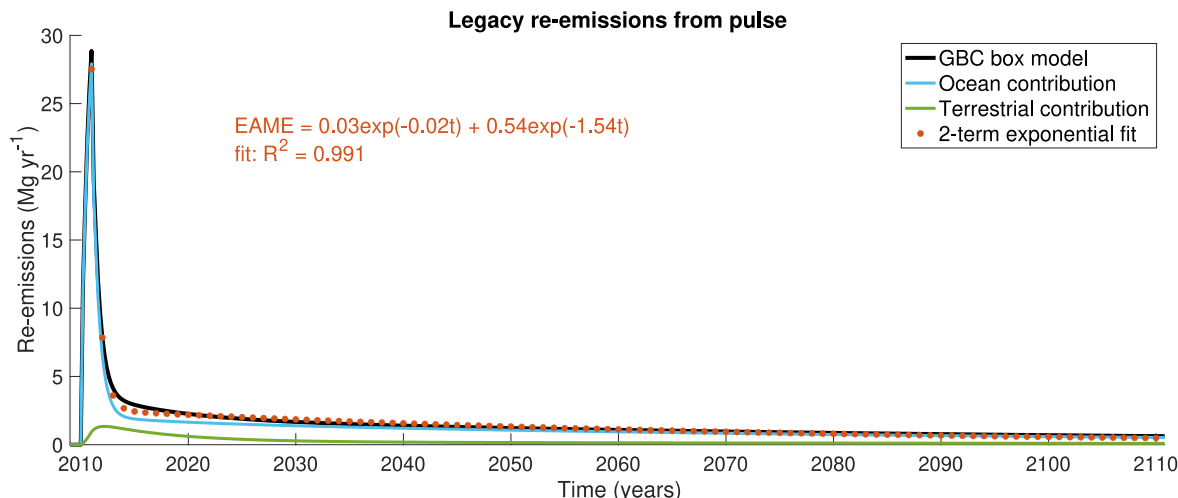
125
 126 **Figure S3.** Generalized additive model (GAM) regional trends for multisite deseasonalized total gaseous
 127 mercury (TGM) data in Eastern North America (A) and Northern Europe (B). The GAM mean estimate is
 128 shown as a black line, with shaded grey areas showing ± 2 standard errors in the GAM estimate. Linear
 129 regression trends (red dashed lines) were calculated over the 2005–2020 period from the regional
 130 nonlinear GAM curve.

131
 132 **Section S4. Calculating EAME equations from the GBC box model and perturbation analysis**

133 We followed the approach of Selin (14) to calculate parameters from the EAME equation (Eq. 2) using
 134 pulse simulations in the Hg Global Biogeochemical Box model (GBC) (15, 16). We introduced an
 135 atmospheric Hg pulse of 100 Mg in the year 2010 and monitored the evolution of legacy re-emissions for
 136 100 years, until 2110 (Figure S4). The two-term exponential model fits the behaviour of the box model
 137 very well ($R^2 \sim 0.99$) on the 100-year time period of the simulation. This fitting reduces the ~ 40 parameters
 138 of the GBC model to 4 understandable parameters, as well as reducing the computation time for legacy
 139 re-emissions. We performed a similar experiment by modeling the release of a riverine pulse, and
 140 evaluated changes to legacy re-emissions. This equation will differ from the atmospheric pulse, as
 141 different timescales are involved (river transport *versus* deposition to oceans) and only a fraction of the
 142 riverine pulse will reach the open ocean and not be buried on the coastal shelf.

143
 144 To estimate a reasonable range in the legacy re-emission pulse parameters (Eq. 2), we performed 1000
 145 parameter perturbation simulations in the GBC model. The 40 relevant parameters that we varied are 35
 146 rate coefficients, 3 parameters for the designation of deposition into soil pools, 1 parameter for geogenic
 147 emissions, and 1 parameter for the fraction of riverine particulate Hg reaching the open ocean. These
 148 parameters were perturbed simultaneously by factors varying between 0.5 and 2, with Latin Hypercube
 149 sampling (17) used to ensure that the parameter space is better explored. For each of the 1000
 150 experiments, we calculated the legacy re-emission pulse parameters (Eq. 2) and selected the 5th–95th
 151 percentile of each parameter as the range for simulations in the 3-box atmospheric model (Table S2). The
 152 1000 experiments were conducted twice, once for atmospheric pulses and once for riverine pulses. The
 153 code for conducting sensitivity experiments in the GBC model is available here:

154 <https://github.com/arifein/gbc-boxmodel-sensitivity>.



155
 156 **Figure S4.** Example of fitting the GBC model pulse experiment to Eq. 2. The contribution of ocean and
 157 terrestrial legacy re-emissions to the total are shown as blue and green lines.
 158
 159

160 **Section S5. 3-box atmospheric model parameter variations**

161 The bounds for the 19 parameters that were varied in the 2×10^5 simulations, along with their
 162 justifications, are listed in Table S2. We sampled the fraction of Hg emitted in the short timescale (f_{short})
 163 and the total re-emissions (E_{total}) instead of the coefficients a_1 and a_2 in Eq. 2. This is less likely to lead to
 164 unrealistic combinations of the a coefficients and the b lifetimes. Integrating Eq. 2 between time 0 and
 165 infinity yields an equation for E_{total} :

$$E_{\text{total}} = a_1 b_1 + a_2 b_2 \quad (\text{Eq. S2})$$

167 The fraction of Hg emitted in the short timescale is equal to:

$$f_{\text{short}} = \frac{a_1 b_1}{a_1 b_1 + a_2 b_2} = \frac{a_1 b_1}{E_{\text{total}}} \quad (\text{Eq. S3})$$

169 We calculated the a coefficients from the sampled variables (b_1 , b_2 , f_{short} , E_{total}) using Eq. S4 and Eq. S5:

$$a_1 = \frac{E_{\text{total}} f_{\text{short}}}{b_1} \quad (\text{Eq. S4})$$

$$a_2 = \frac{E_{\text{total}} (1 - f_{\text{short}})}{b_2} \quad (\text{Eq. S5})$$

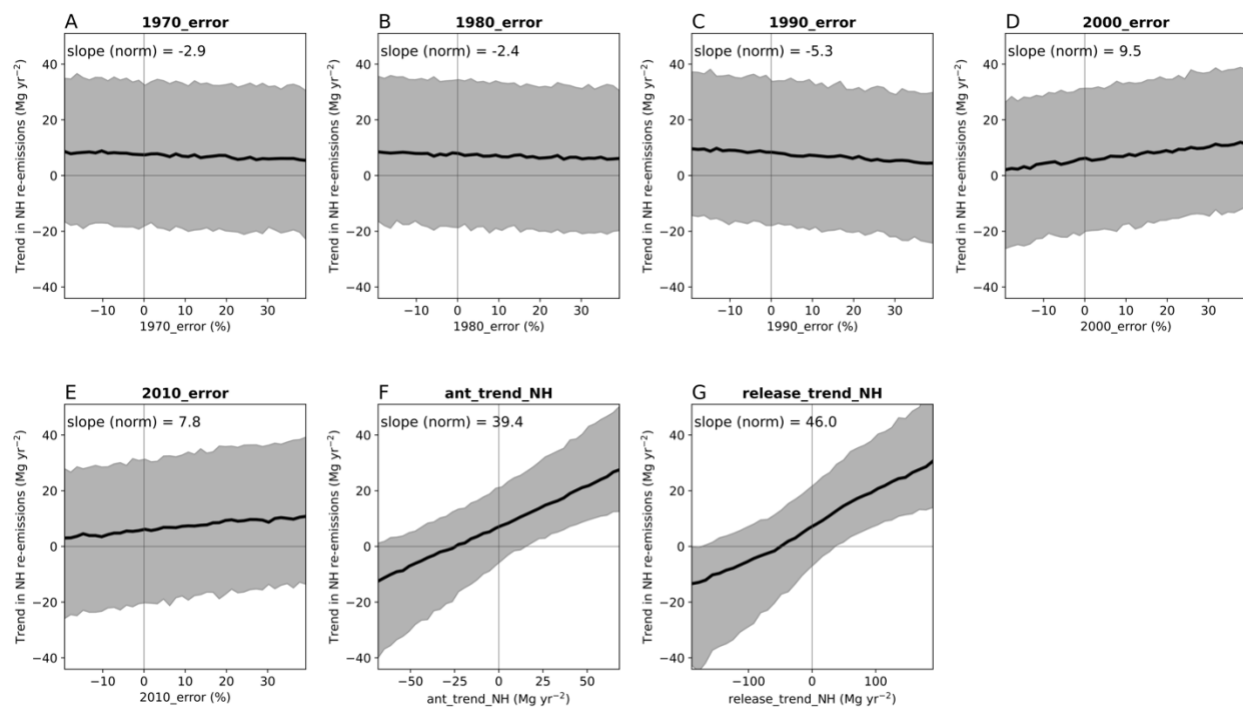
172 The relationships between Northern Hemisphere (NH) Hg re-emissions trends (2005–2020) and
 173 anthropogenic emissions and releases parameters in the 3-box model results are plotted in Fig. S5.
 174

175 **Table S2.** Bounds of parameters varied for the 2005–2020 simulations in the 3-box atmospheric model.

Parameter	Min	Max	Units	Comment/References
Atmospheric Hg lifetime	3	8	months	Horowitz et al. (18); Parrella et al. (19); Zhang et al. (20)
Error in 1970 emissions and releases	-20	+40	%	Error range suggested for 2000, 2010, 2015 emissions in Streets et al. (21)
Error in 1980 emissions and releases	-20	+40	%	Error range suggested for 2000, 2010, 2015 emissions in Streets et al. (21)
Error in 1990 emissions and releases	-20	+40	%	Error range suggested for 2000, 2010, 2015 emissions in Streets et al. (21)
Error in 2000 emissions and releases	-20	+40	%	Error range suggested for 2000, 2010, 2015 emissions in Streets et al. (21)
Error in 2010 emissions and releases	-20	+40	%	Error range suggested for 2000, 2010, 2015 emissions in Streets et al. (21)
Legacy short lifetime (b_1) (atmospheric pulse)	5.7	14.6	months	Based on perturbation analysis of Amos et al. (15, 16) GBC model (Section S4)
Legacy long lifetime (b_2) (atmospheric pulse)	28.6	96.9	years	Based on perturbation analysis of Amos et al. (15, 16) GBC model (Section S4)
Legacy fraction emitted in short timescale (atmospheric pulse)	7	31	%	Based on perturbation analysis of Amos et al. (15, 16) GBC model (Section S4)
Total re-emissions from initial pulse (atmospheric pulse)	79	379	%	Based on perturbation analysis of Amos et al. (15, 16) GBC model (Section S4)
Legacy short lifetime (b_1) (riverine pulse)	1.6	9.5	months	Based on perturbation analysis of Amos et al. (15, 16) GBC model (Section S4)
Legacy long lifetime (b_2) (riverine pulse)	1	116.9	years	Based on perturbation analysis of Amos et al. (15, 16) GBC model (Section S4)
Legacy fraction emitted in short timescale (riverine pulse)	5	55	%	Based on perturbation analysis of Amos et al. (15, 16) GBC model (Section S4)
Total re-emissions from initial pulse (riverine pulse)	2	160	%	Based on perturbation analysis of Amos et al. (15, 16) GBC model (Section S4)
Difference in percent GEM emitted from anthropogenic sources between 2020 and 2005	-20	20	%	The speciation of emissions in longest available inventory (22) varied by 15% (from 60% GEM in 1970 to 75% GEM in 2010)
Anthropogenic emissions trend in Northern Hemisphere (NH)	-70	70	Mg yr ⁻²	Covers wide range without 2020 emissions becoming negative
Anthropogenic emissions trend in Southern Hemisphere (SH)	-10	10	Mg yr ⁻²	Covers wide range without 2020 emissions becoming negative
Deviation of releases trend from emissions trend in NH	-80	80	Mg yr ⁻²	For example, if NH emissions trend is 30 Mg yr ⁻² , the NH releases trend ranges between -21 and 139 Mg yr ⁻² *
Deviation of releases trend from emissions trend in SH	-35	35	Mg yr ⁻²	For example, if SH emissions trend is -10 Mg yr ⁻² , the SH releases trend ranges between -45 and 25 Mg yr ⁻² †

176 * In the NH, decadal release trends in Streets et al. (23) are $1.97 \times$ emissions trends ± 80

177 † In the SH, decadal release trends in Streets et al. (23) are $1.03 \times$ emissions trends ± 35



178
 179 **Figure S5.** The relationships between Northern Hemisphere (NH) Hg re-emissions trends (2005–2020)
 180 and anthropogenic emissions and releases parameters. Plots show the relationship for (A) the error in
 181 emissions and releases for 1970 in the Streets et al. (23) inventory; (B) the error in emissions and
 182 releases for 1980; (C) the error in emissions and releases for 1990; (D) the error in emissions and
 183 releases for 2000; (E) the error in emissions and releases for 2010; (F) the trend in anthropogenic NH
 184 emissions for 2005–2020; (G) the trend in anthropogenic NH releases for 2005–2020. Black lines show
 185 median responses and the shaded area shows the 90% confidence interval (5th to 95th percentile). The
 186 slope (normalized to the range of the x-axis parameter) is listed on the plot to illustrate the relative
 187 importance of a parameter.

188
 189

190 **Section S6. Description of GEOS-Chem simulations**

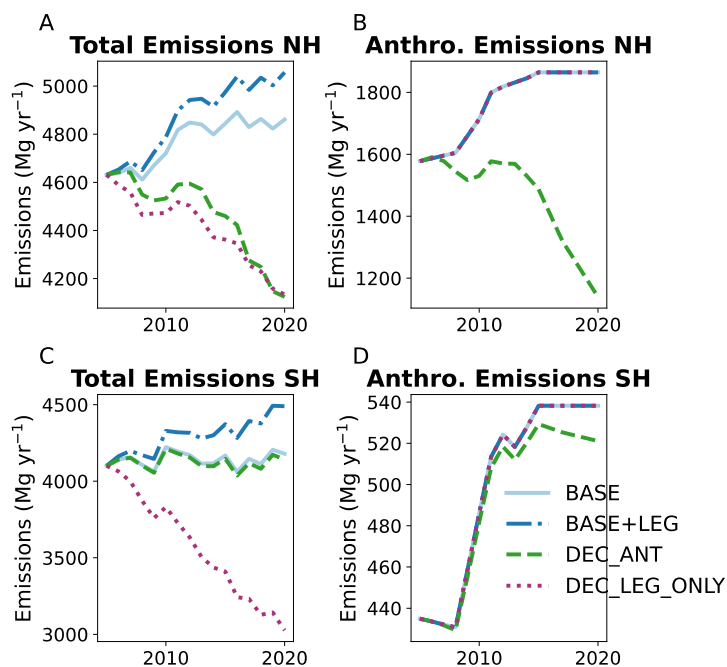
191

192 **Table S3.** Description of Hg simulations conducted in GEOS-Chem for 2005–2020.

Simulation	Anthropogenic emissions	Legacy re-emissions	Overall NH emissions trend (Mg yr ⁻²)
BASE	2005–2015: Streets et al. (21) 2016–2020: repeat 2015	Constant interannually; based on Horowitz et al. (18)	+18
BASE+LEG	2005–2015: Streets et al. (21) 2016–2020: repeat 2015	Trend from median response to BASE anthropogenic emissions trend (Fig. S5F)	+31
DEC_ANT	South and East Asian emissions from BASE are scaled by Chinese emission inventory trend (24)	Trend from median response to DEC_ANT anthropogenic emissions trend (Fig. S5F)	-33
DEC_LEG_ONLY	2005–2015: Streets et al. (21) 2016–2020: repeat 2015	Decline imposed	-30

193

194



195

196 **Figure S6.** The emission timeseries in GEOS-Chem simulations for 2005–2020: total emissions in the

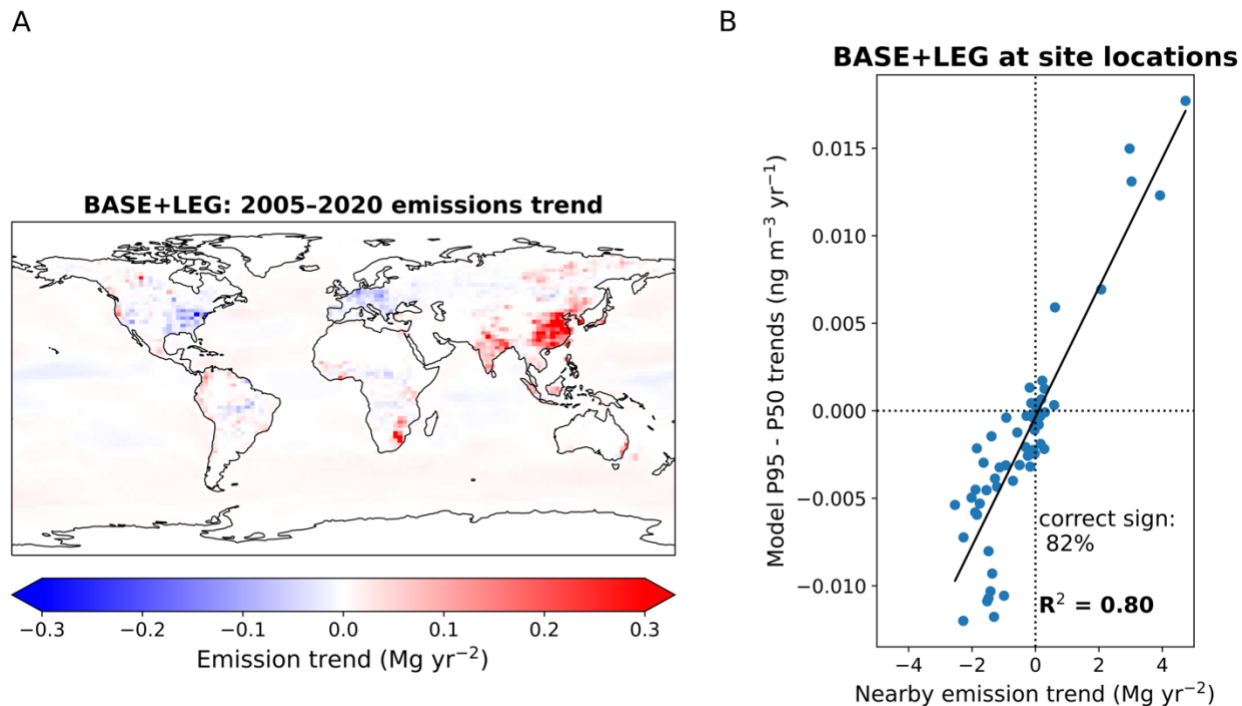
197 Northern Hemisphere (A), anthropogenic emissions in the Northern Hemisphere (B), total emissions in

198 the Southern Hemisphere (C), and anthropogenic emissions in the Southern Hemisphere (D).

199

200

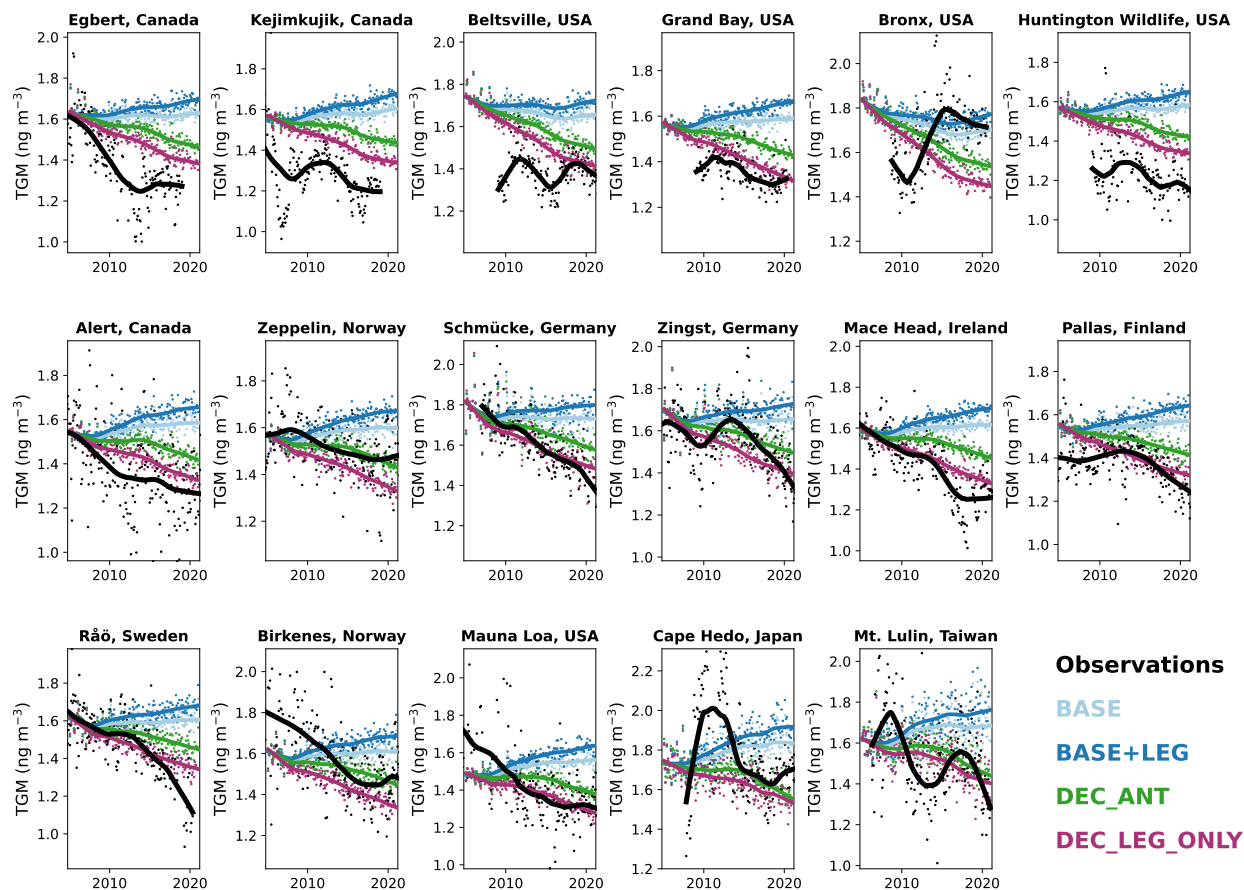
201 Section S7. Correlation between trends in emissions and quantile trends
 202



203
 204 **Figure S7.** Map of the linear trend of Hg emissions in the BASE+LEG simulation between 2005 and 2020
 205 (A). Comparing the relationship between the BASE+LEG simulated nearby emission trend and the
 206 difference between the 95th percentile (P95) and median (P50) quantile regression trends at grid boxes
 207 corresponding to site locations (see Fig. 4C for the full P95 – P50 trends map). The nearby emission
 208 trend is calculated by summing emissions trends within two grid boxes (~500 km) of the site location grid
 209 box.
 210
 211

212 Section S8. Additional comparisons between observations and model simulations

213



214

215 **Figure S8.** Timeseries plots comparing model simulations (colors) and observations (black) at stations
 216 with more than 12 years of data during 2005–2020. Markers show deseasonalized monthly means and
 217 lines show the smoothed tendency of the time series calculated using LOWESS (locally weighted
 218 scatterplot smoothing) regression.

219

220 **Supplementary References**

221 1. M. Iturbide, *et al.*, An update of IPCC climate reference regions for subcontinental analysis of
 222 climate model data: definition and aggregated datasets. *Earth Syst. Sci. Data* **12**, 2959–2970
 223 (2020).
 224 2. D. A. Gay, *et al.*, The Atmospheric Mercury Network: measurement and initial examination of an
 225 ongoing atmospheric mercury record across North America. *Atmos. Chem. Phys.* **13**, 11339–11349
 226 (2013).
 227 3. F. Carbone, *et al.*, Sea surface temperature variation linked to elemental mercury concentrations
 228 measured on Mauna Loa. *Geophys. Res. Lett.* **43**, 7751–7757 (2016).
 229 4. F. Sprovieri, *et al.*, Atmospheric mercury concentrations observed at ground-based monitoring sites
 230 globally distributed in the framework of the GMOS network. *Atmos. Chem. Phys.* **16**, 11915–11935
 231 (2016).
 232 5. A. Cole, *et al.*, A Survey of Mercury in Air and Precipitation across Canada: Patterns and Trends.
 233 *Atmosphere* **5**, 635–668 (2014).
 234 6. V. L. St. Louis, *et al.*, Atmospheric Concentrations and Wet/Dry Loadings of Mercury at the Remote
 235 Experimental Lakes Area, Northwestern Ontario, Canada. *Environ. Sci. Technol.* **53**, 8017–8026
 236 (2019).

- 237 7. K. Tørseth, *et al.*, Introduction to the European Monitoring and Evaluation Programme (EMEP) and
 238 observed atmospheric composition change during 1972–2009. *Atmos. Chem. Phys.* **12**, 5447–5481
 239 (2012).
- 240 8. L. S. P. Nguyen, G.-R. Sheu, D.-W. Lin, N.-H. Lin, Temporal changes in atmospheric mercury
 241 concentrations at a background mountain site downwind of the East Asia continent in 2006–2016.
 242 *Science of The Total Environment* **686**, 1049–1056 (2019).
- 243 9. K. Marumoto, *et al.*, Long-Term Observation of Atmospheric Speciated Mercury during 2007–2018
 244 at Cape Hedo, Okinawa, Japan. *Atmosphere* **10**, 362 (2019).
- 245 10. Y. Zhang, *et al.*, Observed decrease in atmospheric mercury explained by global decline in
 246 anthropogenic emissions. *Proc. Natl. Acad. Sci. U.S.A.* **113**, 526–531 (2016).
- 247 11. K.-L. Chang, *et al.*, Trend detection of atmospheric time series. *Elementa: Science of the*
 248 *Anthropocene* **9**, 00035 (2021).
- 249 12. S. N. Wood, Fast stable restricted maximum likelihood and marginal likelihood estimation of
 250 semiparametric generalized linear models. *Journal of the Royal Statistical Society (B)* **73**, 3–36
 251 (2011).
- 252 13. K.-L. Chang, M. G. Schultz, G. Koren, Selke, Niklas, Guidance note on best statistical practices for
 253 TOAR analyses. Available at: <https://doi.org/10.48550/arXiv.2304.14236> (2023).
- 254 14. N. E. Selin, A proposed global metric to aid mercury pollution policy. *Science* **360**, 607–609 (2018).
- 255 15. H. M. Amos, D. J. Jacob, D. G. Streets, E. M. Sunderland, Legacy impacts of all-time anthropogenic
 256 emissions on the global mercury cycle. *Global Biogeochem. Cycles* **27**, 410–421 (2013).
- 257 16. H. M. Amos, *et al.*, Global Biogeochemical Implications of Mercury Discharges from Rivers and
 258 Sediment Burial. *Environ. Sci. Technol.* **48**, 9514–9522 (2014).
- 259 17. M. D. McKay, R. J. Beckman, W. J. Conover, Comparison of Three Methods for Selecting Values of
 260 Input Variables in the Analysis of Output from a Computer Code. *Technometrics* **21**, 239–245
 261 (1979).
- 262 18. H. M. Horowitz, *et al.*, A new mechanism for atmospheric mercury redox chemistry: implications for
 263 the global mercury budget. *Atmos. Chem. Phys.* **17**, 6353–6371 (2017).
- 264 19. J. P. Parrella, *et al.*, Tropospheric bromine chemistry: implications for present and pre-industrial
 265 ozone and mercury. *Atmos. Chem. Phys.* **12**, 6723–6740 (2012).
- 266 20. Y. Zhang, *et al.*, An updated global mercury budget from a coupled atmosphere-land-ocean model:
 267 40% more re-emissions buffer the effect of primary emission reductions. *One Earth* **6**, 316–325
 268 (2023).
- 269 21. D. G. Streets, *et al.*, Global and regional trends in mercury emissions and concentrations, 2010–
 270 2015. *Atmospheric Environment* **201**, 417–427 (2019).
- 271 22. M. Muntean, *et al.*, Evaluating EDGARv4.tox2 speciated mercury emissions ex-post scenarios and
 272 their impacts on modelled global and regional wet deposition patterns. *Atmospheric Environment*
 273 **184**, 56–68 (2018).
- 274 23. D. G. Streets, *et al.*, Five hundred years of anthropogenic mercury: spatial and temporal release
 275 profiles. *Environ. Res. Lett.* **14**, 084004 (2019).
- 276 24. K. Liu, *et al.*, Measure-Specific Effectiveness of Air Pollution Control on China’s Atmospheric
 277 Mercury Concentration and Deposition during 2013–2017. *Environ. Sci. Technol.* **53**, 8938–8946
 278 (2019).